• U C •

FCTUC FACULDADE DE CIÊNCIAS
E TECNOLOGIA
UNIVERSIDADE DE COIMBRA

DEPARTAMENTO DE
ENGENHARIA MECÂNICA

Development and Construction of a Device Related to a New Structured Metallization Concept for Back-Contact Crystalline Silicon Solar Cells by using Metal Foil

Dissertation Submitted in Partial Fulfillment of the Requirements of the Degree of Master of Mechanical Engineering at the Field of Energy and Environment

Author

Alexander Rui Pfaff Mayer

Advisors

Pedro Mariano Simões Neto

Jan-Frederik Nekarda

Jury

President	**Professora Doutora Ana Paula Betencourt Martins Amaro** **Professor Auxiliar da Universidade de Coimbra**
Vocals	**Professor Doutor Pedro de Figueiredo Vieira Carvalheira** **Professor Auxiliar da Universidade de Coimbra**
Advisor	**Professor Doutor Pedro Mariano Simões Neto** **Professor Auxiliar da Universidade de Coimbra**

In collaboration with

Fraunhofer ISE

Fraunhofer Institut für Solare Energiesysteme
Freiburg i. Br.

Coimbra, February, 2014

Acknowledgments

The work that is here presented would not be possible without the encourage and support of some people, I would like to thank for.

To Pedro Neto, my thesis advisor and friend at Coimbra University, for the mentoring even from a far distance.

To Jan Nekarda and Andreas Rodofili for this fantastic opportunity to work on Fraunhofer ISE, improving my knowledge on photovoltaic and their laser processing.

To the entire Laser Team from OE751 where I have past much time over this year and always carry a good working atmosphere: Carmen, Susana, Christian, Andi, Artur, Simon, Martin, Uli, Markus, Gisela, Fabi, Moritz, Rene and Falah. Thanks for the nice teamwork!

To the team of the mechanical workshop at Fraunhofer ISE, who converting my designed pieces of chuck into reality. Special thanks also to Csaba for his helpfull advices during this time.

Markus Klawitter, for his support and explanation on the field of numerical simulation.

To Bishal Kafle for his help by the final corrections and the great Nepalese food!

To my longtime friends Paulo Oliveira, André Gourgel, Dane Detelic, João Santos, Pedro Ramos, Vasco Simões and José Gomes, who pushed me forward over my academically journey.

And at last I want to thank to my lovely family.

Resumo

Os processos de fabrico referentes à metalização em células solares de alta eficiência têm um elevado impacto no seu custo global de manufatura. Em particular a metalização de células em silício cristalino do tipo *Back-Contact* mostra-se ser difícil e, desta forma, um problema do ponto de vista industrial.

Este trabalho de tese trata do desenvolvimento de um dispositivo projetado para realizar e avaliar o potencial de um novo conceito de metalização destinado à face traseira de células do tipo *Back-Contact*. Aqui, a formação dos eletródios em padrão, baseia-se em contactar e estruturar uma folha de alumínio através de aplicação a laser. De forma a garantir um bom contacto metálico, o dispositivo desenvolvido deverá primeiramente assegurar uma boa fixação da folha de alumínio com o substrato, assim como um bom desempenho para a posterior estruturação da folha. Desta forma serão criados os contactos metálicos seletivos. Entretanto, os principais desafios tecnológicos enfrentados durante o desenvolvimento do dispositivo serão identificados e corrigidos.

Este aparelho foi desenvolvido e testado no Fraunhofer Instituto de Sistema Energéticos Solares ISE em Friburgo, Alemanha.

Por fim, foram ainda efetuados ensaios com o dispositivo, tirando-se as primeiras conclusões acerca do desempenho deste novo conceito de metalização. Serão apresentadas algumas sugestões para futuras investigações nesta área.

Palavras-chave: metalização, células fotovoltaicas de alta eficiência, *back-contact*, folha de alumínio, aplicação a laser, silício.

Abstract

Metallization and contacting processes have a significant impact on the total manufacturing cost of the high-efficiency solar cells. The metallization of silicon crystalline back-contact solar cells is difficult and still a major issue from the industrial point of view.

The core of the current thesis introduces the development of a device, designed to realize and evaluate the potential of a new rear side metallization concept for back-contact cells. Here, the formation of the electrode pattern is based on contacting and structuring a metal foil through a laser processing scheme. In order to ensure a good metallic contact, the developed device shall first assure a safe foil fixing and later an appropriate handling for structuring the metal foil in order to make selective metallic contacts. Meanwhile, the major technological challenges faced during the device development are identified and assessed.

Finally this device has been developed and tested at the Fraunhofer Institute for Solar Energy Systems ISE in Freiburg, Germany

An overall conclusion of the experimental findings has been made and an outlook for further investigations required in this field has been proposed at the end of this document.

Keywords: metallization and contacting, high-efficiency solar cells, back-contact, laser applications, metal foil, silicon.

Table of contents

LIST OF FIGURES

LIST OF TABLES

SYMBOLS AND ACRONYMS

Symbols

Variable	Description	Unity
A_1	outlet area	[m²]
A_2	inlet area	[m²]
A_{foil}	area of foil	[m²]
A_{ring}	area of the suction ring	[m²]
$\vec{E}$	electrical field	[N/C]
E_G	band gap	[eV]
Eg_{si}	Band gap of silicon	[eV]
E_{ph}	photon energy	[J]
F_{foil}	Force acting on foil	[N]
h^+	hole	[eV]
I_{SC}	short-circuit current	[A]
I_{mpp}	short circuit current	[A]
L_F	length of the contact	[m]
R_P	parallel resistance	[Ω]
R_s	series resistance	[Ω]
V_{OC}	open-circuit voltage	[V]
V_T	thermal voltage	[°C]
V_{mpp}	voltage at maximum power point	[V]
e^-	Electron	[eV]
n_0	Reflectance index	
n_1	Reflectance index	
n_2	Reflectance index	
p^-	under pressure	[bar]

p^+	over pressure	[bar]
p_{atm}	atmospheric pressure	[bar]
ϕ_{nozzle}	Nozzle diameter	[m]
ϕ_{spot}	Contact spot diameter	[µm]
h	planck's contant	[Js]
FF	fill factor	[%]
Si	silicon	
SiO_2	Silicon oxide	
T	absolut temperature	[°C]
V	voltage	[V]
c	speed of light	[m/s]
d	Distance	[m]
k	Boltzmann constant	[J/K]
pi	pitch	[m]
q	electron charge	[C]
t	time	[s]
v	velocity	[m/s]
Δp	Pressure difference	[bar]
η	Efficiency	[%]
λ	Wavelength	[nm]
ξ	Resistance number	
ρ	density	[g/m³]
υ	photon frequency	[Hz]

Acronyms

ARC – Anti-Reflection Coating

BC – Back-Contact

CFD – Computational Fluid Dynamics

EWT – Emitter Wrap Through solar cell

IBC – Interdigitated Back Contact solar ell

ISE – Institute for Solar Energy Systems

LFC – Laser-Fired Contacts

MWT – Metal Wrap Through solar cell

$PECVD$ – Plasma Enhanced Chemical Vapor Deposition

$PERC$ – Passivated Emitter and Rear Cell

$mc - Si$ – Multicrystalline Silicon

FVM – Finite Volume Method

FDM – Finite Difference Method

$Al - BSF$ – Aluminum Back Surface Field

PV – Photovoltaic

$e - h\ pair$ – electron-hole pair

LIP – Light Induced Plating

1. INTRODUCTION

Facing the circumstances that population is continuously growing and at the same time the human living standards all over the world are growing, energy consumption and their demand is rising faster than expected. Energy is nowadays an indispensable good to life standards and economic growth. Food production, mobility and illumination are only some of many sectors where energy in form of electricity is required. Today most electricity is obtained by fossil resources extracted from earth reserves, which will run out soon. Besides that, its negative environmental impact makes clear that competitive secondary energy sources need to be reinforced and extended. This issue of energy demand can only be covered by a non-centralized junction of other sources, preferentially with a clean and non-exhaustible origin.

Today, renewable energies are getting even more interesting for high scale energy production thanks to their raising efficiencies and competitiveness comparing to conventional sources like oil, coal and nuclear energy. This is visible by its growing market share and their establishment in the energy sector. Because of their non-exhaustible nature, they are seen as a good complement for future energy deficits. Considering the free and incredible high volume of sun light that hits earth day by day (Figure 1-1), it would be a pity not to exploit this amount of energy to cover part of humans' energy necessity. Therefore the research on photovoltaic takes a responsible part to the positive development of the renewable energy sector.

Since the first build silicon solar cell in 1953 [1], a huge technology leap has happened in this area. Over the last 20 years, thanks to innovative manufacturing processes, solar cells became more efficient, cheaper and cleaner than in the past. It is remarkable that 10 years ago there was not even a 2 GWp worldwide total installation of photovoltaic modules; today it is above 108 GWp.

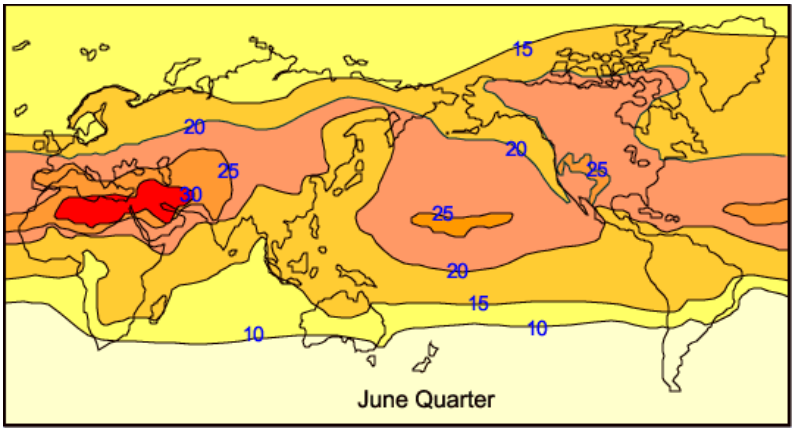

Figure 1-1: Exemplary average of global solar irradiation per day on the second quarter in year (June Quarter). The units are in MJ/m² and give the solar insolation falling on a horizontal surface per day [2].

Eicke Weber, the director of the Fraunhofer Institute for Solar Energy Systems ISE, expressed his ambitious belief that "in 10-15 years PV-generated electricity will be cost competitive with fossil and nuclear electricity" [3].

Recent prognoses indicates good progress, however this tendency only can fulfil the goal of a stronger photovoltaic presence, by discovering new cell concepts and competitive manufacturing processes for a new and more efficient cell generation. The reduction of the cost per Watt-peak of solar energy is one of the main focal points of present solar cell research. Regarding to the future of crystalline silicon solar cells, two points are decisive:

- Existing technologies need to be more efficient and drag down production cost.
- New or already existing high-efficiency cell concepts need to be industrial feasible.

One high-efficiency cell structure, whose development has reached a viable industrial implementation, with the potential to supersede the actual standard industrial Al-BSF solar cell in the coming years, is the *Passivated Emitter and Rear Cell (PERC)* design. New contacting technologies, such as Laser-Fired Contact (LFC) have possibly a simpler and faster contacting method than before for this cell type.

Another cell design with high potential is the *Back-Contact cell* design, although until now its actual metallization procedure is expensive and thus non-profitable

for mass production. Here innovative metallization methods need to be developed to bring these cell design steps closer to industrialization.

1.1. Motivation and objective

The aim of this work consists of verifying the implementation of a new and reproducible metallization concept for back-contact crystalline silicon solar cells, based on a laser contacting application with metal foil.

Here it was required to design and construct a wafer chuck device, which performs the contacting and structuring of metal foil onto a wafer substrate. Hence, after its laser contacting application, an important and challenging step during this process chain is to produce an air gap between the wafer and the aluminum foil. This requires a controlled foil elevation in-between its contacts.

The expectations of this work are a successful handling of the designed chuck such as positive first experimental results. To guaranty an unproblematic execution of the concept process, the adhesion of the foil onto the wafer such as the possibility to elevate the foil near the contacts, has to be certified.

In resume, this can be a good alternative to the currently used structured metallization forms for industry application, which are expensive and with many complex processing steps involved.

1.2. Structure of thesis

This present work is divided in five chapters.

The 1st and 2nd chapter relates the motivation and fundamental principles of crystalline silicon solar cells. This will help to understand the functionality of energy conversion and their body structure. Furthermore a short preface of the most promising high-efficiency cells, PERC and Back-Contact, such as the common manufacturing techniques to create a structured metallization at the rear side of Back-Contact cells is mentioned.

The 3rd chapter presents the design of a device for new and alternative solutions of structured metallization using metal foil. Based on the LFC technology, the chuck has to be able to hold the foil safe and tight to the wafer, while at a further step foil is elevated for structuring. Its design development is presented and its mechanical challenges such as their resolutions are referred.

Furthermore an evaluation of the device is executed and results of first experimental test are provided.

In the 4th chapter the experimental procedure is explained, as well as its component arrangement. Measurements of the foil surface topography during the foil elevation step were recorded and its results discussed.

In the 5th chapter it will be given the overall conclusion of this metallization concept and suggestions for future work.

2. THEORY AND TECHNOLOGY OF CRYSTALLINE SILICON SOLAR CELLS

In this chapter the fundaments of solar cells and its constitution are set.

First it is explained the physical basics of cell technology, the conversion background of sunlight into electrical energy and furthermore the design of two high-efficiency cell concepts with prior interest to this work are discussed.

Continuing with solar cell fundamentals, it follows the common actual metallization processes for crystalline silicon back-contact solar cells existing meanwhile under research, such as their influence by the cell development. This chapter closes with the foil as a metallization alternative contacted by laser application, which together are the principal motivation for this work.

2.1. Principles of photovoltaic

2.1.1. Semiconductor, photons and generation

Crystalline silicon solar cells own its name due to the nature they are primarily constituted of. *Silicon* (Si) is a semiconducting material that belongs to the IV period table group; and crystalline, due to its crystalline lattice structure. Like all materials that belong to the group of semiconductors, it is their *band gap* that distinguishes them from conducting or non-conducting (isolator) materials. The definition of band gap is given as the distance between the highest energy state in the *valence band* and lowest energy band in the *conduction band* of a solid-state material. Hence the minimum energy an electron, located at the valence band, needs to jump out of its covalent bonds and reach the conduction band, corresponds to the *forbidden gap* E_g. When this happens the electron is at a higher level, where it behaves similar to a free electron and so is able to attribute to the charge transport, leaving a *hole* at its place which is also free to move. In this case it's the mention of an *electron-hole pair*.

While valence and conduction band on conducting materials overlap, they do not possess any band gap and so no fully occupied shell; in non-conducting materials the

band gap is too large ($Eg > 5$ eV) and therefore the conduction band almost unreachable for excited electrons. Semiconductors on the other hand have an $Eg < 5$ eV, what possibly them the particularity to behave as a non-conductor, or rather as conducting material. For silicon in particular, energy has to be higher than $Eg_{Si} = 1.107$ eV.

A photon transports an energy E_{ph}, which is determined by its wavelength, and can be calculated using the formula:

$$E_{ph} = h\upsilon = \frac{h \cdot c}{\lambda} \tag{2.1}$$

where, h is the Planck's constant, υ is the frequency of photon, c is the speed of light in vacuum and λ is the photon's wavelength.

Therefore, photons with large wavelength ($E_{ph} < E_g$) interact only weakly with the semiconductor, while photons with energy greater than the bandgap energy ($E_{ph} > E_g$) are more likely to create electron-hole pairs. This phenomenon is called the *photovoltaic effect* and it was first observed in 1839 by Becquerel [4]. This is illustrated in Figure 2-1.

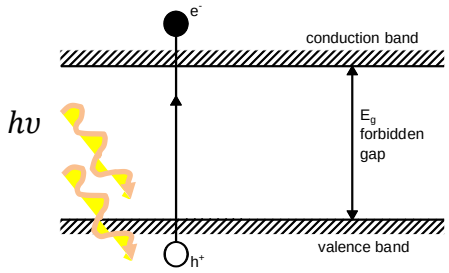

Figure 2-1: Electron-hole pair generation when illuminated with light of energy $\boldsymbol{E_{ph} = h\upsilon}$, where $\boldsymbol{E_{ph} > E_g}$ (according to [5]).

Energy can be applied in form of light or heat, conductivity is strongly affected also by temperature, increasing with this. However, in its pure state semiconductors by themselves are neither good insulators nor good conductors. To increase the carrier density, impurity atoms with one more or one less valence electron than the semiconductor can be added to the material, forming an n-type material or a p-type material, respectively. This process is called *doping*. The illustration in Figure 2-2 shows the atomic difference between two doped materials.

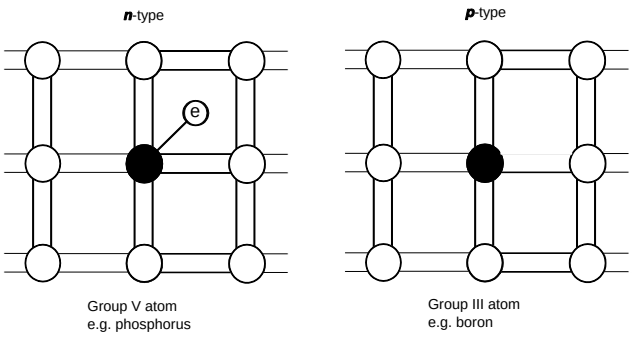

Figure 2-2: Schematic representation of a silicon crystal doped with impurities to produce n-type and p-type semiconductor material (according to [5]).

2.1.2. The p-n junction

Any semiconductor used for electrical purpose is normally composed by at least two oppositely doped regions: a p-type doped region and an n-type doped region.

Once these two regions are joined together, the concentration gradient between excessive number of holes at one side and electrons at the other side, leads to *diffusion*. The diffusion occurs across the junction and by leaving ionized atoms on either side, an *electrical field* $\vec{E}$ is created. Its opposite orientation difficult the diffusion process and by gaining force, less mobile carries are capable to cross the junction. At certain point the force is such that a dynamic equilibrium is reached. The region in were this equilibrium is established is named the *depletion zone* because there are no remaining free charge carrier at this region to carry the current.

As soon as the junction is thereupon submitted to irradiation, electron-holes pairs are generated and due to $\vec{E}$, forced to spread opposite directions. Hence a current flow I is originated so the charge carriers get collected at the surfaces and wander through the metal contacts to the consumer load. Figure 2-3 summarizes the p-n junction.

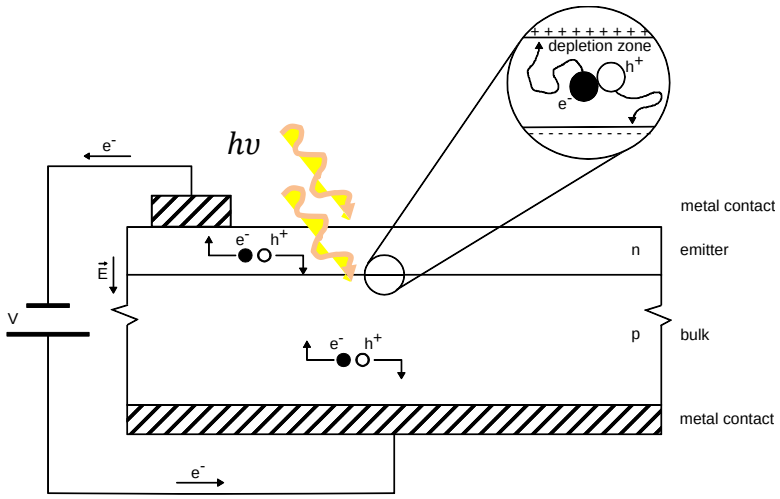

Figure 2-3: Circuit flow of p-n junction at a classical solar cell design (according to [5]).

To reduce the recombination[1] rate of the carriers, a thin passivation layer is applied onto the surface of the cell. The most usual passivation[2] are done by depositing a thin film layer of aluminum oxide, silicon oxide or silicon nitride onto the wafer surface.

2.1.3. Light trapping

As sunlight is made of a large wavelength spectrum range, going from several hundreds of nanometers till several micrometers, when exposured over an active cell surface, photons can get reflected, absorbed or transmitted. Since energy conversion is directly connected with the irradiated area and its light capture, the absorption rate of photons influences immensely its efficiency yield. Hence to maximize the power rating of a solar cell, it must be designed so as to maximize its light absorption, so they can generate a higher amount of charge carriers.

To increase surface light absorption or either decrease light reflectance, an *anti-reflection coating (ARC)* is applied as well as a *random pyramid texture* is etched onto the active surface. This additional cell treatments can reduce its surface reflection from 30% to 10% or even below [5]. At Figure 2-4 both light trapping methods are schematically illustrated.

[1] Recombination is when electron-hole pair, after its generation meet up and reunify before getting collected.
[2] Passivation is a dielectric layer, applied on cell surface to prevent surface recombination.

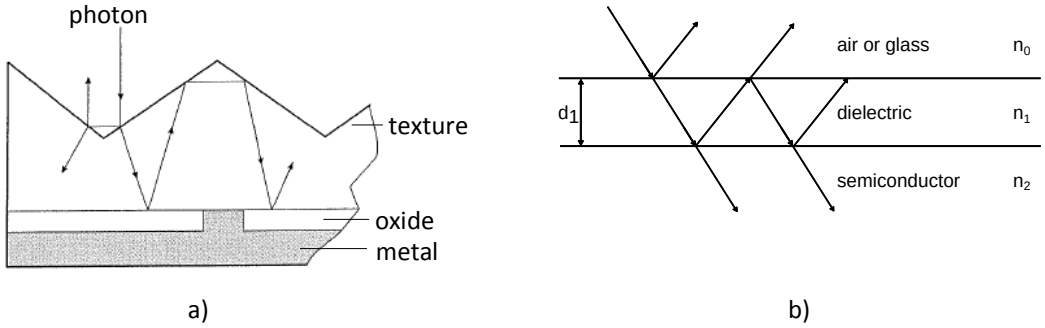

Figure 2-4: Light trapping methods for reducing the incident light reflection; a) pyramid texture on the photoactive surface [6]; b) trajectory of photon through an anti-reflection coating with thickness $\boldsymbol{d_1}$ and where $\boldsymbol{n_0}$, $\boldsymbol{n_1}$, $\boldsymbol{n_2}$ are the refractive indexes of the corresponding materials (according to [5]).

2.1.4. Two-Diode Model

Generally a solar cell is nothing else than a large area diode. One of the most accurate models to describe its electrical behavior is the two diode model. It is based on the diode equations of Shockley and traduces the physical meanings into mathematical equations. In its equation it also considers resistive losses, as the serial and the shunt resistance, as well as the recombination current I_{02} originating from the recombination in the depletion zone. This makes it a highly accurate way to determinate the major cell parameters. Figure 2-5 shows the equivalent electrical circuit of a solar cell based on the two-diode model.

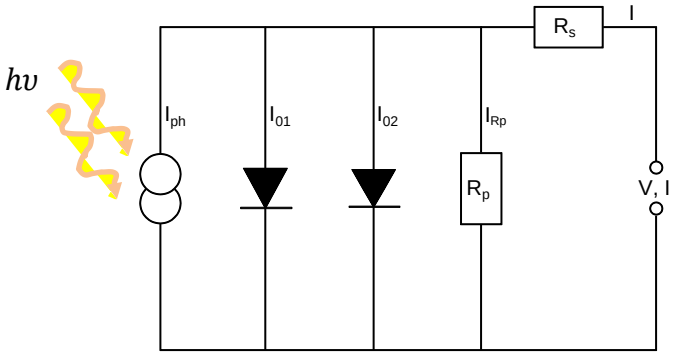

Figure 2-5: Equivalent circuit diagram for the two-diode model in a real solar cell [7].

where I_{ph} is the short circuit current generated by light irradiation, I_{01} and I_{02} are the two diode saturation currents, R_p is the shunt parallel resistance and R_s is the series resistance.

The current $I(V)$ of an irradiated cell is given by:

$$I(V) = I_{01} \cdot \left(e^{\frac{V - I(V)R_s}{n_1 V_T}} - 1 \right) + I_{02} \cdot \left(e^{\frac{V - I(V)R_s}{n_2 V_T}} - 1 \right) + \frac{V - I(V)R_s}{R_p} - I_{ph} \qquad (2.2)$$

here n_1 and n_2 are the diode ideality constants and $V_T = kT/q$ is the thermal voltage, where k is the Boltzmann's constant, T is the absolute temperature and q is the charge of an electron. The major contributors to the series resistance are the bulk resistance of the semiconductor material, the metallic contacts and interconnections, carrier transport through the top diffused layer such as the contact resistance between the metallic contacts and semiconductor.

The Figure 2-6 represents a typical I-V characteristic curve for dark as well as illuminated cells. The illuminated characteristic curve belongs to the fourth quadrant, since the generated current of a solar cell flows in the opposite direction to the diode current. Due to the integration of (2.2) the current I_{mpp} and the voltage V_{mpp} at the maximum power point P_{mpp} are obtained. Further parameters are the short circuit current I_{SC} and the open circuit voltage V_{OC}.

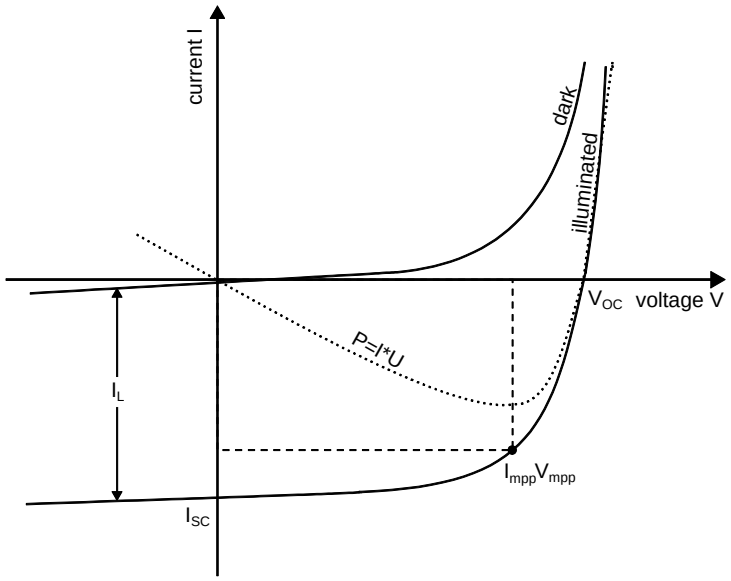

Figure 2-6: Typical representation of the dark and illuminated $\boldsymbol{I-V}$ characteristic curve of a crystalline silicon solar cell. $\boldsymbol{I_{SC}}$ represents the short-circuit current, $\boldsymbol{V_{OC}}$ the open circuit voltage, $\boldsymbol{P}$ is the generated cell power and $\boldsymbol{V_{mpp}}$, $\boldsymbol{I_{mpp}}$ are, respectively, the voltage and current on the maximum power point.

Open circuit voltage V_{OC} is the maximum voltage, at zero current.

Short circuit current I_{SC} is the maximum current of a solar cell and occurs when the voltage is zero.

Maximum power point P_{mpp}, is where the product of I and V is maximum (V_{mpp}, I_{mpp}). It is the optimal operating point of the solar cell.

The *Fill Factor* FF, is a further quantity that compares the maximal convertible power P_{mpp}, with the product of I_{SC} and V_{OC}.

$$FF = \frac{I_{mpp} V_{mpp}}{I_{SC} V_{OC}} \tag{2.3}$$

in other words, it describes the squareness of the $I - V$ curve.

The most important property for global evaluation of a solar cell is its efficiency η. It is defined as the ratio between the maximum generated photoelectrical power P_{out} and the incoming photon power P_{in}, and quantifies the fraction of solar energy that it converts into electrical energy:

$$\eta = \frac{P_{\text{out}}}{P_{\text{in}}} \Rightarrow \eta_{\max} = \frac{P_{mpp}}{P_{ph}} = \frac{V_{mpp} \cdot I_{mpp}}{P_{ph}} = \frac{V_{OC} \cdot I_{SC} \cdot FF}{P_{ph}} \tag{2.4}$$

hence the efficiency of a solar cell is directly dependent on the open circuit voltage, short circuit current and fill factor.

2.2. Cell concepts

This section introduces two promising designs of high-efficiency cells that are nowadays under investigation and have contributed to this work.

High efficiency solar cells are cells with special treatments where the physical limitations imposed by the classical standard cell structure are overcome. These limitations can be various: they can be due to optical losses such as shadowing, reflection or unabsorbed radiation; they can be electrical losses, for example due to the series resistivity R_s induced by contacts (semiconductor-metal contact, fingers, etc...), or by the existence of recombination losses at the surfaces or in the bulk of the cell [7]. Therefore these kinds of cells often present a more complex structure than the typical industrial cell. These modifications usually result in a final enhanced efficiency, even though they require higher technological efforts.

As it was mentioned before, the PERC cell design is becoming gradually involved into industrial manufacturing. Its design such as the back-contact design, are going to be introduced next.

2.2.1. PERC design

Passivated Emitter and Rear Cell (PERC) solar cells have been first successfully realized in 1980 by Blakers [8]. Figure 2-7 illustrates its particular design. Generally it presents a similar constitution to the actual Al-BSF industrialized standard cell: it is composed by a p-type silicon bulk; presents a thin n-doped emitter at the photoactive surface such as a pyramidal surface texture with an anti-reflection coating; a finger grid contact as font metallization, while at the rear side it is fully metallized. However it differs from the present standard cell in particular by the addition of a dielectric layer at the backside of the cell.

The backside passivation is a thin dielectric layer, which may vary from several nanometers to hundreds of manometers, made of aluminum oxide, silicon oxide or silicon nitride and normally applied through PECVD[3]. The purpose of rear side passivation has two reasons: in one hand, to reduce the recombination rate of the charge carriers by saturating the surface density of states; and on the other hand does it work together with the underneath applied metallization as a mirror for the transmitting light, improving significantly its reflectance quality compared to non passivated designs [9]. The highest efficiency archived on this cell type on a mono crystalline bulk have reached up to 25 % [10].

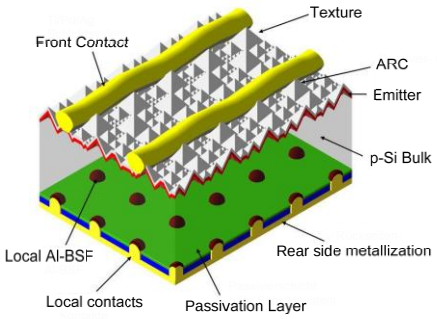

Figure 2-7: Schematically illustration of the Passivated Emitter and Rear Cell (PERC) structure [11].

Since the dielectric passivation layer has isolator properties, it is necessary to create local openings for establishing the electrical contact between silicon and electrode.

[3] PECVD is the short for **P**lasma **E**nhanced **C**hemical **V**apor **D**eposition, which is a thin film deposition technique, where a plasma source enables to deposit gas state materials into solid state on a substrate.

Depending on the metallization type, in most cases it is realized by photolithography structuring or via a laser process. While the first has a higher process quality connected to higher complexity and cost, the second one is more efficient, faster and therefore industrial more attractive.

2.2.2. Back-Contact design

Comparing to conventional bifacial metalized PV cell structures like the PERC design, an interesting and particular cell design is presented by the Back-Contact cell family. Here, the main difference consists on the arrangement of the electrical contacts. Since the contact grid on each cell, consisting of busbars and fingers, induces optical losses by shadowing 3.5% and 4.5%, respectively [12], the intention on this design is to minimize these optical losses. Hence instead of representing contacts on both cell surfaces, the polarities are majorly located and connected at the back side of the cell given by a pattern of finger electrodes.

The advantages are more than auspicious: reduction or even complete elimination of shading losses due to the absence of the metallization grid and the busbars at the front side. As result of more light absorption, a higher cell current generation I_{SC} can be achieved. Furthermore higher module compactness can be reached and easier interconnections between cells are possible, thus less serial resistance losses in tabs.

Mainly there are three different back-contact cell types which are being under investigation. A single description is given below such as the respective architecture is illustrated in Figure 2-8.

- *Emitter Wrap Through (EWT)* cell – at this structure, holes are drilled by laser through the bulk to the back side. The openings are after all emitter diffused, enabling a vertical formation of the p-n junction. To collect the charge carriers at the bottom of the cell an interdigitated n-p metal pattern is, at this surface, required (Figure 2-8-a).
- *Metal Wrap Through (MWT)* cell – at this structure the aim is to transfer the large front side busbars[4] back to the rear side of the cell and therefore minimize the part of the shadowing losses. Holes drilled

[4] Busbars are the main finger lines of any electrode which does the cell interconnection. Their function is to collect generated current from the finger grid and transport this out the cell.

through the solar cell will function as a conductive bridge for front side generated carriers. With this feature, busbars at the front side can entirely be placed to the rear side of the cell while the finger grid maintains at the front. Hence an interdigitated conduction pattern is required at the back surface (Figure 2-8-b).

- *Interdigitated Back Contact (IBC)* or *Back Contact Back Juntion (BCBJ)* cell – At this particular kind of structure the rear surface is selective and interdigitated p and n doped. The entire p-n junction is located at the back side of the cell. This way all generated current is collected at the back side of the cell, hence the complete finger grid at the front side is transferred to the rear surface. This cell structure has demonstrated very high conversion capacities (Figure 2-8-c).

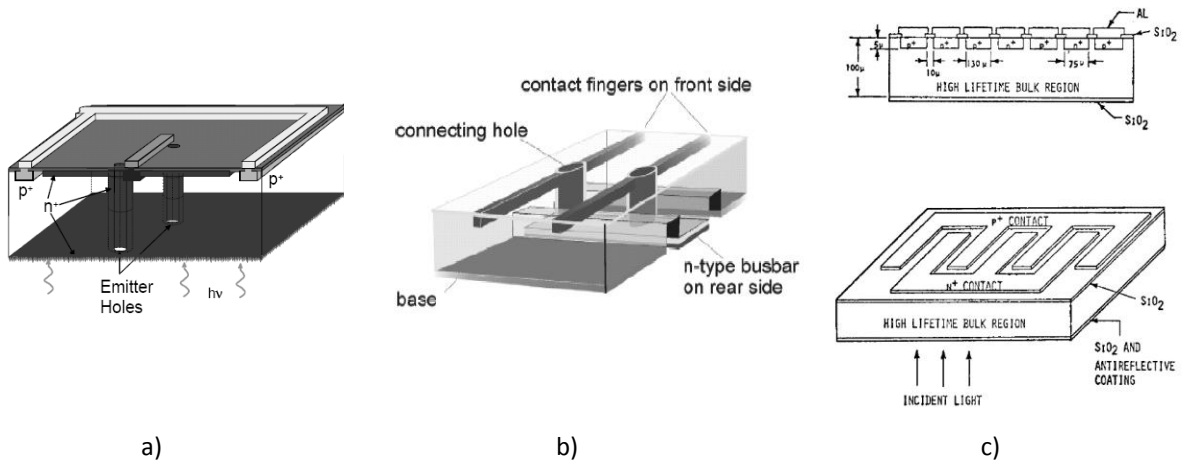

a) b) c)

Figure 2-8: Illustration of the three main back-contact structures: a) The Emitter Wrap Trough cell (upside down) [13]; b) The Metal Wrap Through cell [14]; c) The Interdigitated Back Contact cell (upside down) [15].

A first IBC cell was commercially realized by the SunPower Corporation and it shows impressive conversion efficiency above 23.7 % [16]. Though, in general this cell design is not yet adapted for large scale manufacturing. Its metallization in form of an interdigitated grid of p and n electrodes is not competitive and economically viable for mass production. This represents the major success barrier of this cell design today.

2.3. Manufacturing techniques for Back-Contact electrodes

In this section it will be focused on the common metallization techniques for silicon back-contact solar cells. Meantime they are the industrial screen printing, vapor deposition and plating.

Several metallization methods exist to apply a metal layer at the rear surface of a crystalline silicone solar cell. Considering a passivated and interdigitated doped back surface, the metallization procedure can occur after, or before the contacting procedure between the metal layer and the subjacent wafer is established. Here, multiple solutions and process combinations are available, like etching, firing, laser ablating or directly laser firing. For this work only the last, the LFC technique is relevant (see section 2.4), for its fundamental know-how contribution to this work.

The main difference of the back –contact cell designs, comparing to the conventional cell design, is that both electrode polarities are located on the rear side of the cell. Hence their shape is in form of narrow fingers, interdigitated and isolated between polarities. Next are defined the main techniques for creating finger grid contacts at the rear solar cell surface.

2.3.1. Screen printing and firing

Screen printing [17] is the oldest and most applied metallization technology for crystalline silicon solar cells, hence it is also known as the standard metallization technique for the front side finger grid and back side full area metallization. This thick film technology has the advantage to transfer any desired metallization pattern onto a wafer surface, what makes of it a good metallization all-rounder.

The flat-bed printing mechanism is the most widely spread way of industrial cell printing. The key elements for screen printing are the screen (that defines the pattern), the paste (that defines the metal) and the squeegee. In Figure 2-9 the screen printing procedure is represented. It first starts by dispensing the paste onto the screen and applying a pressure to the squeegee. This puts the screen in contact to the underlying wafer substrate. As following step, the squeegee is moved from one end to the opposite, dragging and pressing the paste continuously till the end. Reaching this point screen is elastically

retired. At the locations there was a gap in the screen, the paste has filled and left a negative screen print on the wafer.

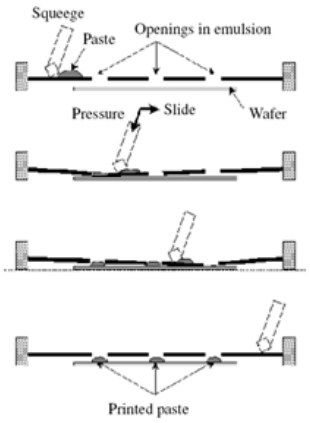

Figure 2-9: Illustration of the flat-bed screen printing technique.

After applying the metal layer, the printed paste needs to accomplish a final thermal treatment for establishing the contacts and harden out. This process step is called the *firing* step and it improves the electrical conductivity by melting the glass frites and firing through the passivation layer. Industrially this occurs at an in-line belt furnace, where the wafers transit three heat stages. On the first stage, wafers are submitted to a surrounding atmosphere temperature below $600°C$. Here, organic components isolated in between the metallic paste or attached to the wafer surface, are burned out. By the following stage, temperatures rise above 660°C during [time]. In this short period metal powder starts to melt diffuses with the silicon surface, originating a si-metal alloy. It's at the third and last firing step, when temperatures are below 577°C, the melted alloy solidify with the eutectic composition, creating a good ohm resistance.

The main disadvantages of this technique are the electrical conductivity limitation set by the composition of the paste, which are non-conductive. More implications that cannot be avoided by this method are the mechanical and thermal stresses that act on the substrate during the metallization. Furthermore, the imprecise alignment of the grid and its constraint in matters of narrowed contacts can rapidly cause to shunts. An alternative contacting method to firing after the screen printing metallization, is contacting via laser firing [18].

2.3.2. Physical Vapor Deposition structuring and Plating

In photovoltaic another well-known technique to apply a metal layer onto a surface substrate is by physical vapor deposition. In order to archieve a structured electrode, the full area layer has to be structured in subsequent process steps. Afterwards the electrodes can be thickened by plating to achieve sufficient conductivity. As this occurs under high vacuum, atoms bounce with thermal energy against the semiconductor substrate and condensate on this afterwards. The evaporating source can be generated in distinct forms. The most common forms of PVD in photovoltaic are resistively heated sources (Figure 2-10-left) and electron beam heated source. Another PVD technique is by sputtering (Figure 2-10-right). Here high-energy particles are fired upon a sputter target surface, whereby their material atoms get pulled out as result of the collision and move in high velocity onto the substrate and condensate as a thin film. Beside the high adjacent costs interconnected to the energy wasted for high vacuum medium of $0.05\ mbar$, vapor deposition technique is today an indispensable method when the requirements of good homogeneity, adhesion and thin layer deposition qualities are specified [19].

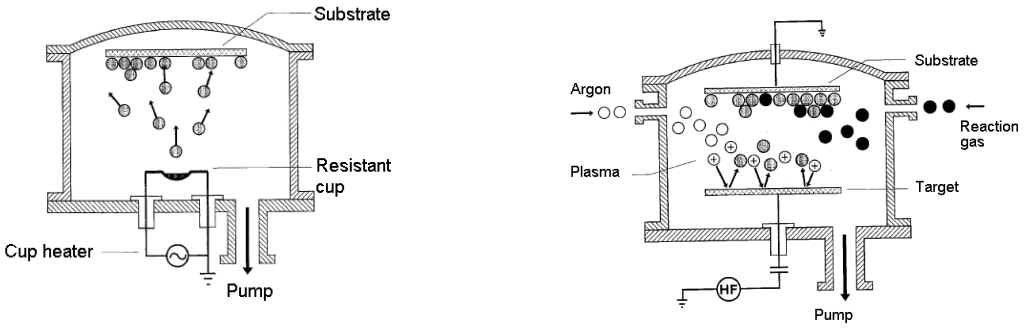

Figure 2-10: Thin metal layer deposition through the thermal PVD. A resistant cup with the depositing metal is thermal evaporated (left) and sputtering (right) [19].

The second method is by plating. This one works more on a chemical way of deposition, since the substrate is immersed in a suitable metal ion bath. Here metal ions (anode) in the electrolytic bath will be reduced to solid metal and deposited onto the substrate (cathode) so as to form an adhering layer thereon. The thickness of the deposited metal layer is dependent of the time the substrate is dipped in the bath. Furthermore, depending on the depositing metal and substrate, it can be distinct between electro plating and electroless plating. Electroless plating, is similar to the first, however, it uses a chemical deposition process instead of an external electrical circuit.

Since electroplating technique needs a metal seed as guide line, to create a certain metallization grid pattern on the wafer surface with high quality, PVD and plating methods are combined in the same process flow. Additionally the finger structure is drawn by several etching steps or by laser ablation.

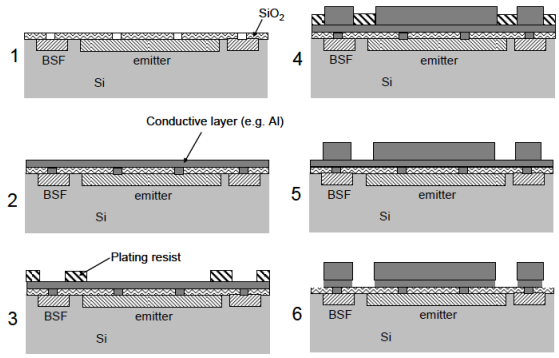

Figure 2-11: Metallization technique for commercial IBC cells patented by Sunpower [20].

Figure 2-11 illustrates the interdigitated metallization technique of the unique commercialized back-contact cell from Sunpower which is patented by Mulligan et al.[21]. Here first a thin seed (metal layer) is vapor deposited onto the rear cell surface and afterwards a plating resist is applied locally where the separation between the metal fingers is required, on the top of the metal layer. It follows a thickening process of the metal layer by electroplating, using Ag or Cu plating baths. After the plating resist is stripped, it follows a wet chemical etching were the thin metal layer between the thick plated metal fingers can be etched away [20].

2.4. Laser-Fired contacts with Al-Foil as metallization technique

Another way of metallization, though yet only for full-area metallization, is the foil technique [22]. Here a metal foil is applied onto the rear wafer surface which is afterward contacted by laser application.

Compared to other metallization techniques, foil has its major advantages due to the facility of acquisition such as its implementation in industrial scale. Delivered on a bush, it is easy to fit on any roll-to-roll system. The foil itself is made of an 99% aluminum alloy what gives it good electrical properties and it can be acquired in a wide range of

thicknesses as widths. Moreover it offers good optical properties due to its reflective surface and the presence of air in-between foil and bulk.

The contact is established by a laser based application named *Laser-fired contact* (LFC). It enables attaching and contacting the foil to the si-bulk through localized contact spots. This contacting technology was first introduced by Schneidelöchner and Preu [23] in 2001 at the Fraunhofer ISE and after in 2002 patented by Preu [24]. Today this feature of LFC process enables fabrication of p-type solar cells that reach 22.0 %. This technology permits metallizing and contacting at a very fast rate and in merely one step high-efficiency cell structures with rear side passivated surfaces (PERC).

3. STRUCTURED METALLIZATION FOIL CHUCK DESIGN

In this Chapter it is clarified the mindset and the development of the chuck device for foil metallization in structured form. The origin of concept has its roots at the full area Foil-LFC process and is somehow a further application of it. The respective explanation and similarities of these two processes are given below.

To realize the application of this concept idea, a chuck device was developed and constructed having in mind the necessary features that guaranty the realization of it. All particularities of this development are described in the subchapter 3.2, such as first experimental evaluation of the device and concept.

Furthermore, the way of fixing the foil onto the wafer as well as finding a solution for elevating it, brought several challenges. Here the use of computational fluid simulations tool has been used and the improvement of device components was executed to fulfill its task.

3.1. Introduction

Laser-Fired Contacts (LFC) is one possibility for producing solar cells with a standard PERC design. This process demonstrates high potential in matter of cost reduction and process velocity at industrial manufacturing scale. Therefore it is a competitive and attractive process for cells with a dielectric passivation at the back side, PERC [2.2.1]. Hence laser and foil combine very well for contacting, and Back-Contact cells show, as the PERC structure, high efficiencies ability and interesting improvements in matter of industrial scale manufacturing, the idea to create a cheap and quick metallization process for this cell types appeared. Next are presented the single metallization steps of the Foil-LFC for PERC cells, such as of the novel metallization concept for back-contact cells.

3.1.1. Full area Foil-LFC for PERC cells

In this process the rear side of cell is metallized with an aluminum foil. The process runs as followed:

1. The aluminium foil is rolled over the passivated wafer back side and fixed by a vacuum surface located around wafer;
2. A pulsed laser beam in the infra-red spectrum range fires a pattern of point spots which melts the foil and the wafer surface underneath, thus attaching the foil to the substrate and establishing local electrical contacts between Si-bulk and metal foil;
3. The excessive foil is cut out around the wafer through a laser tool.

The Figure 3-1 shows a scheme of the described metallization process.

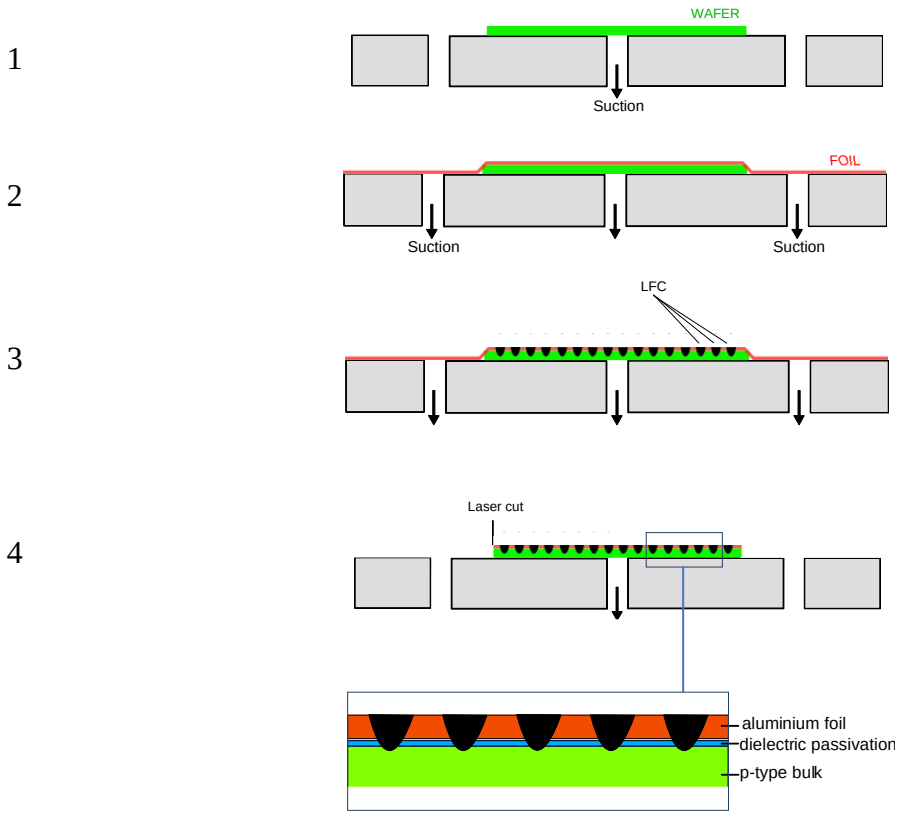

Figure 3-1: Method formation of the back side full area LFC metallization using aluminum foil.

The result of a finish processed cell by this described procedure is pictured in Figure 3-2. Here the front side silver finger grids are formed by screen-printing technique, whereas the back side is full metallized with aluminium foil and laser fired.

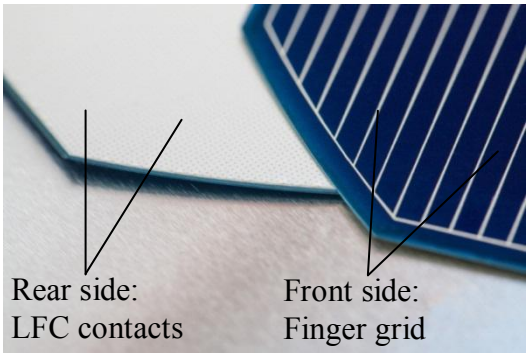

Figure 3-2: Photograph showing an full area Foil-LFC metallization at the rear side and screen printed Ag finger grid at the front side of a PERC cell.

Since this technique show high efficiencies at low processing costs [22], the question appeared if foil could also be used in a similar way to create a structured metallization for the back-contact cells.

3.1.2. Structured Foil-LFC for Back-Contact cells

To create a structured metallization by using foil, a similar process to full area LFC is executed. At the end though, the electrodes need to appear in form of stripes and not in form of a full surface. Only the primal LFC steps are applied, while the firing further processing steps need to be executed for structuring. Aluminium foil is in its original form a full plane roll, stripes has to be cut out after the laser contacting step. Here the corresponding process flow is summarized:

1. The foil is applied over the Si-wafer and fixed due to vacuum surface located around the substrate, just like the first step of the conventional Foil-LFC process;
2. A laser fires contact spots in a sort of a line pattern, with a certain distance between them and parallel to each other;
3. A laser cuts around the contact lines, isolating the individual electrode lines from the neighbouring lines. The result is an equidistant aluminum stripe pattern.

It is important to have in consideration that on step 3, the substrate can suffer thermal damages during the laser incidence. To avoid this negative effect, foil must not be in direct contact with the wafer substrate during this step, except at the contact spots.

A possible way to realize this foil elevation lies on creating an overpressure domain in this region and hence building up an air gap between wafer and foil. This step occurs just after process step 2 and before initiating step 3. As soon as the foil is at a stable displacement to the substrate, process 3 can initiate. The gap size that is referred is in the order of several micrometers just enough to laser beam out of its focus and hence out of a damaging range when incident on the substrate. Figure 3-3 shows the metallization procedure schematically.

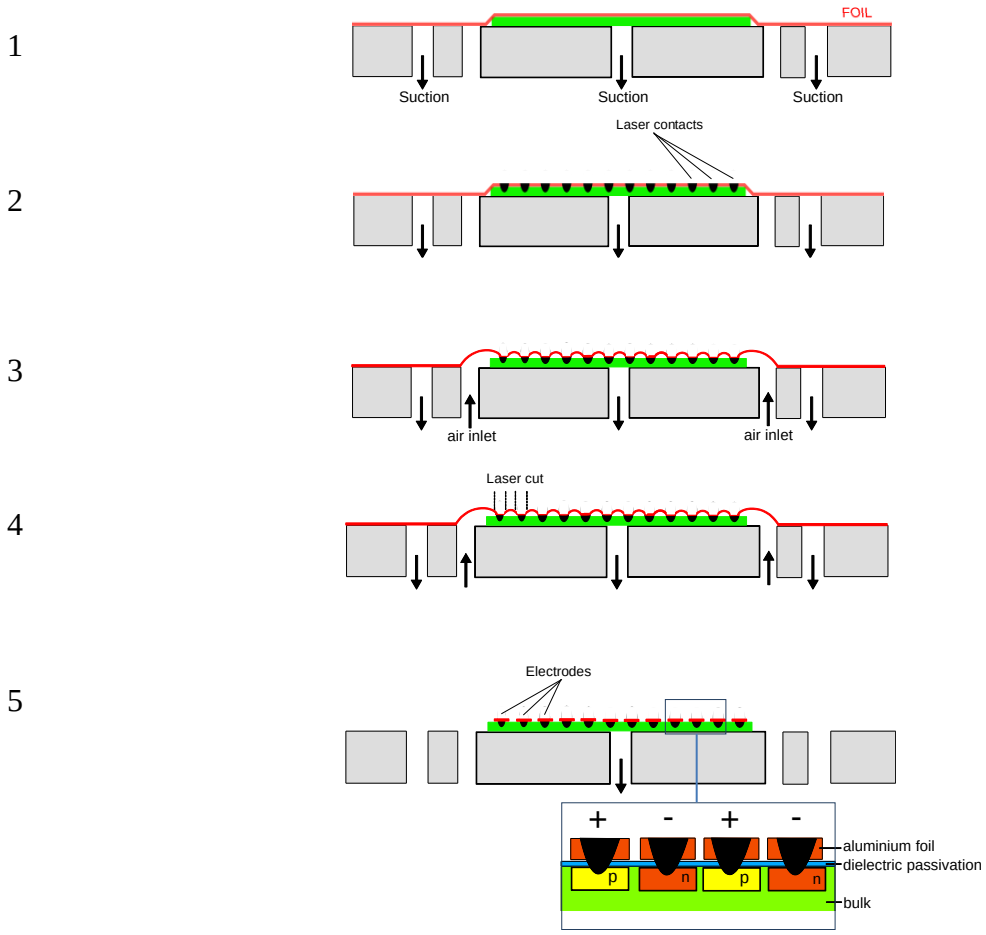

Figure 3-3: Process scheme for creating a structured metallization for back-contact cells using aluminium foil.

The final goal is to become at the end of the process, a rear wafer surface covered with a pattern of narrowed aluminium foil stripes. Each strip only contacted by its firing line and isolated from its adjacent stripes.

3.2. Chuck device development

The design of the chuck device started by collecting all necessary boundary conditions it has to accomplish for its application. Since the vacuum is responsible for the foil fixing as well as for the prevention of foil wrinkle, it has to be kept active during the whole metallization procedure. This means the foil suction and the blow operation are going to work at the same time, although in separate regions. For careful wafer positioning it was also opted for a vacuum fixation. Its thin thickness of 150 to 200 µm, makes of it a highly fragile object. All together the device has to manage the following tasks:

- An area with continuous air suction for attaching and fixing the foil on the wafer without wrinkling it;
- An area with temporary air blowing to create an overpressure region;
- An area with continuous air suction for wafer holding and positioning.

To satisfy the above edited requirements, the device had to be constituted of three independent air flow zones. In the middle area the wafer is positioned for processing. At the outer area with suction properties, the foil is fixed by a vacuum frame. The region with blowing properties is placed in between the foil suction and wafer suction. The Figure 3-4shows the design principle of the device to be developed.

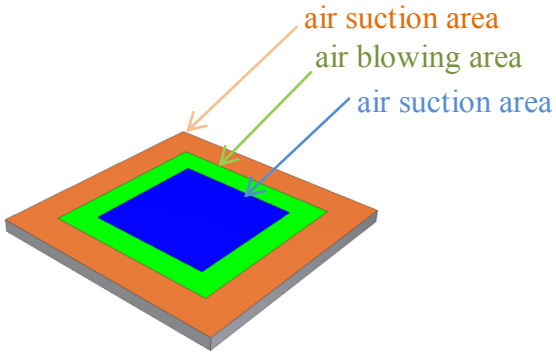

Figure 3-4: Sketch of the two frames concept. Beside the area where the wafer overlie (blue), there is an outer frame for foil suction (orange)and an inner frame for air blowing (green).

Once defined its functionality, the body dimensions were identified. The procedure takes place in a laser workstation made by the German laser manufacturer Innolas Systems GmbH. The model is the 500 X and was especially designed for high-

precision applications for several material processing, including photovoltaic. The developing device has to respect the installation size to fit into the workstation. At the workstation the device is positioned on a mounting plate (Figure 3-15 – right), which on this part is fixed on linear motorized xy- stages. Dimensional limitation is set by the lack of space inside the working area of the automated equipment. Hence two wafer pickers limit the altitude (Figure 4-1) and the lateral limits established due to the XY-stage border range. Figure 3-5 represents these limitations schematically.

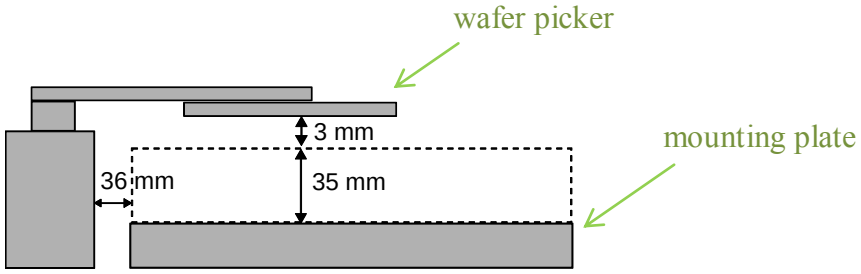

Figure 3-5: Space limitations to be considered for the dimensional design of the chuck (not to scale).

Specified the body dimensions of the device, a more integral study of its sectioned areas followed. As the wafer has well-defined dimensions, the surface and therefore its suction area, has to adopt same dimensional values. The outer frame on the other hand, to guaranty a strong foil adhesion onto the device surface and wafer, follows the pressure equation:

$$p = \frac{|\vec{F}|}{A} \tag{3.1}$$

where, F is the force magnitude applied perpendicular onto the foil's surface with area A, at a pressure p. Since the pressure which exercised onto the foil is defined by the vacuum pump, the force that acts on the foil is directly proportional to A. Hence, for a good foil adhesion the suction area (and therefore the frame) has to be maximized.

To evaluate the inner frame, it is important to consider the strain that act on the foil during its inflating operation. Figure 3-6 represents a simplified illustration of the ideal case when air is inflated into the wafer area. Here suction and overpressure generate forces with opposite directions loading on the foil.

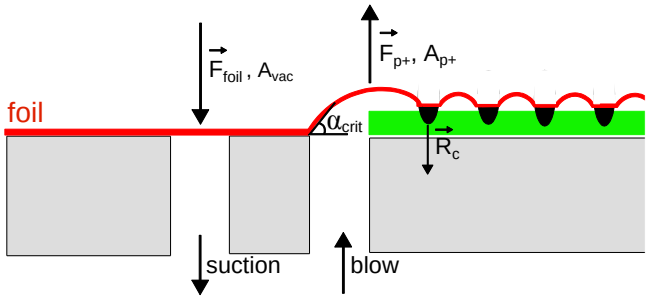

Figure 3-6: Simplified schematic illustration of the foil and its loading forces during the inflating phase (ideal case). $\vec{F}_{foil}$ is the load acting on the foil, A_{vac} is the suction area, $\vec{F}_{p^+}$ is the force acting on the inflated foil zone, A_{p^+} is the foil area exposed to the inflated zone, $\vec{R}_c$ is the reactive force on the outer contacts and α_{crit} is the angle that the foil does with the horizontal in the delimitation between inflating and suction area.

As for the vacuum frame, the force magnitude that is applied on the inflating foil F_{p^+}, is proportional to its area A_{p^+} at a given pressure p. Since this area will always be greater than the area in between contact lines, the shear stresses, which act on the outermost contact lines, are proportional to the force and so to its area. To minimize the strain between foil and contacts, the area A_{p^+} has to be minimized. With this, the dimensioning of the three area need to be as followed: the inner area has got a settled wafer area, the inner frame, with the blowing action, has to be compact and the outer frame with the suction action, has to be large area. Once defined the rough dimensions of the device, its single functionalities were explored in more detail. The next section relates them in particular.

3.2.1. Multiple Element Assembly

A goal was to build the device in a way of a flexible construction kit that could be easily adapted to different requirements. Hence the device was designed in four individual components. This has the advantage that in case of need to replace any of them by improvement of their design, it won't be necessary to construct an entire new device, but only the respective component. The assembly is composed of the following elements: outer frame element, inner frame element, wafer base element and air duct element.

Outer frame element

This element has the function to spread and hold the foil wrinkle free close to the wafer substrate. Only if the foil lays in directly contact to the wafer without any gap between them, the following laser process can run clearly, by alloying the foil onto the

substrate. If there is no physical contact at the spot, what happens is that the incident laser beam does not attach the foil to the substrate, but merely drills a hole into it. This is an unwanted effect. To obtain a uniform vacuum suction at the whole surface area, the suction area of the frame was made out of a porous material. This material was used before at the foil laminating machine of Klausmann's work [25] and showed a good adherence behavior for the foil. The specifications of this material are given in Table 3-1.

Table 3-1: Properties of the porous material used on vacuum frame [26].

Type	CE 100 White
Porosity	100%
Temperature	100°C
Bending strength	24 N/mm²
Vacuum straining	Good
Average pores diameter	10-12 µm

The Metapor ring was glued onto the outer frame component as shows in Figure 3-7. Beside what was mentioned above, this piece of device has a secondary important function during the course of the process which should not be neglected. It has the function to maintain and isolate the over pressurized volume that is build up during the pressure step. Air can rapidly escape from the overpressure region below the foil if the adherence force is not sufficient to counterforce the induced overpressure. By increasing pressure, air will first tend to escape through weak zones. In these zones, punctual pressure concentrations lead to a breakout of air as soon as the sustainable air pressure limit is reached and the adherence of the foil is lost. Weak zones where this can occur are the inner corners of the suction ring. Since the ideal homogenous pressure distribution, would be by a circular shape, to enable a uniform distribution during the pressurized phase, the inner corners of the suction area have been rounded with a radius of 23 mm. As result, a higher inflating pressure is expected. Figure 3-7 shows the outer frame component.

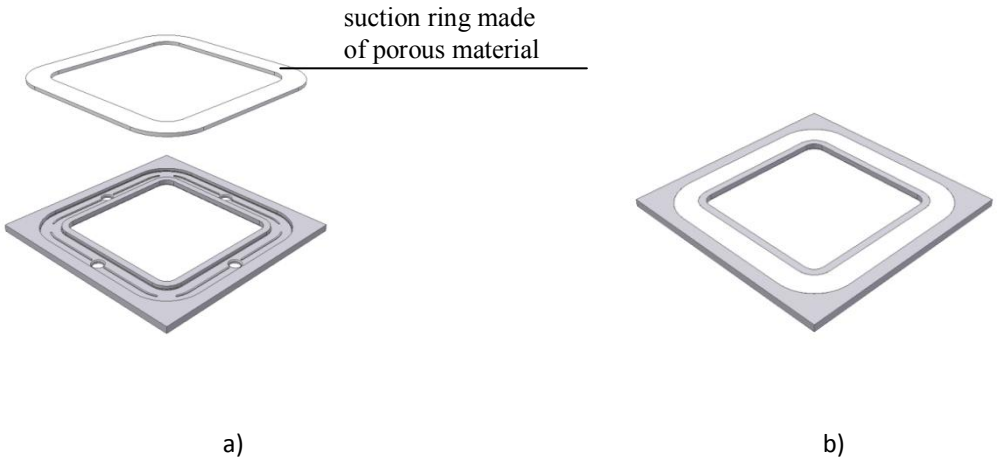

Figure 3-7: a) Explode view of the components outer frame and the porous suction ring with an area of $A_{ring} = 24000\ \mathbf{mm}^2$. b) Final representation of the suction element with rounded inner corners.

Inner frame element

As mentioned before, this component is responsible to create an overpressure region between foil and substrate. It has four air chambers, one on each edge and each of them can work separately since they have separate input channels, which can be controlled separately. Several solutions for the air inlet design have been considered (Figure 3-8).

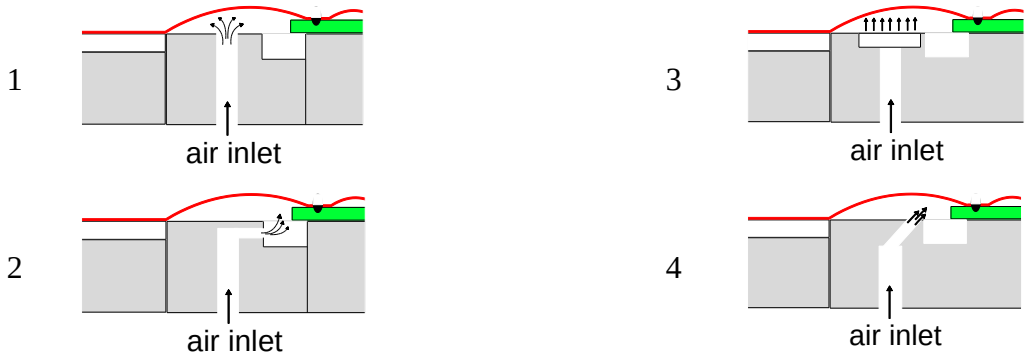

Figure 3-8: Illustration of the several options for air flow directions. 1) With a direct injection; 2) with a side outlet; 3) air flows through porous metapor material to assure constant flow rate; 4) Inclined flow direction.

For the selection of the appropriate solution the air flow direction and the local pressure have been taken into account. One critical zone is definitely the borderline that separates the suction region and holds the foil from the inflating region. In this zone two forces are acting on the foil in opposite directions, which can influence the adherence quality.

Illustration 1 was the first idea that appeared. Given is a simple opening on the surface of the device. The second concept relies on the idea to position the air outlet

opening somewhere not directly exposed to the surface to avoid local pressure concentrations at the foil. A proposal is here a lateral outlet. The third illustration has an even porous surface as the outer frame, although the air flow direction is inverted. The idea behind this concept is to obtain a uniform outgoing air stream. The fourth illustration is represented by an inclined stream outlet. Here the background meaning was to conduct the air directly above the wafer into the volume between the wafer and the foil.

Concerning the optional drawbacks for selection, the drawback of illustration 2 is that it cannot be used as suction component (if necessary), such as the out streaming air can, at worst case, influence the vacuum stability of the wafer. As illustration four is more or less a further development of illustration one, the elected options was number three and four.

As mentioned before, the frame area has an impact on the shear strength and therefore this should be minimized. Hence the frame was designed short and compact.

Figure 3-9: Perspective renders view of the inner frame design.

Furthermore to be sure of a uniform air flow, this component was submitted to an air flow simulation. Since the outlet air flow has an impact on foil deformation, it should be as homogeneous as possible to avoid maxima local pressures.

The section 3.2.2, clarifies in more detail the simulations and subsequent design changes made for this object.

Wafer base element

The next introduced element is the surface that supports the wafer. Its dimensions were adapted to commonly used full-square wafers with dimensions of $(156x156)\ \mathrm{mm}^2$. Though the element surface was shortened to an area of $(154x154)\ \mathrm{mm}^2$, leading to a $1\ mm$ overlap of the wafer over each edge (see Figure 3-10, b). The reason for this shortening was to allow a precisely edge detection by the camera, since the wafer position is a very important factor for laser processing. A second reason for this deepening on the wafers edges was to permit a more careful foil detachment around the wafer, without leaving any metal wastes on the working surface. The element surface in Figure 3-10 illustrates a pattern of drilled holes for fixing the wafer position when vacuum is active.

a) b)

Figure 3-10: Illustration of the wafer-base element: a) Perspective view showing the through-holes pattern; b) Section view where it shows part of a $\mathbf{156x156\ mm^2}$ wafer (green) with an edge overlap of **1 mm** to get an accurate camera positioning detection.

Air-duct element

This element is below the previous three and so it has the function to bring all elements together forming one piece. It also has the function to conduct the air flow into the respective areas. Since there are many air inlets and outlets for guiding the fluid to the respective places, it was necessary to include an air flow channel. To reduce the outlet connections, suction channels have been joined into one access pin. Moreover, outlet channels have been rounded to avoid pressure drops. The end design of this component and its flow directions are illustrated in Figure 3-11.

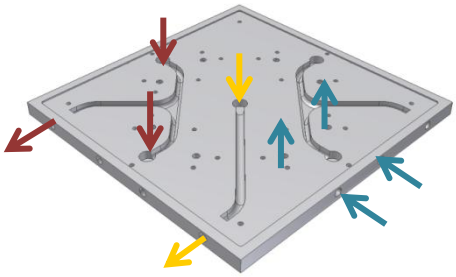

Figure 3-11: Perspective overview of the air-duct element with its respective air channels. The red arrows illustrate the suction air flow such as the yellow for the wafer and the blue arrows represent the incoming air channels.

After assembling the device elements it was crucial to obtain a good surface quality, this means planar and low inclination tolerance overall top surface. Hence having this in mind, the tolerances of the single components had to be little and the screw fittings were located at the back side of the device. To seal the air channels and to guaranty that there is no air leakage between the elements, it was decided for the usage of a Teflon sheet. This material shows good sealing properties, is well machinable and has an adequate stiffness for not influencing the planarity of the device. The Figure 3-12 shows the device split by each of its components.

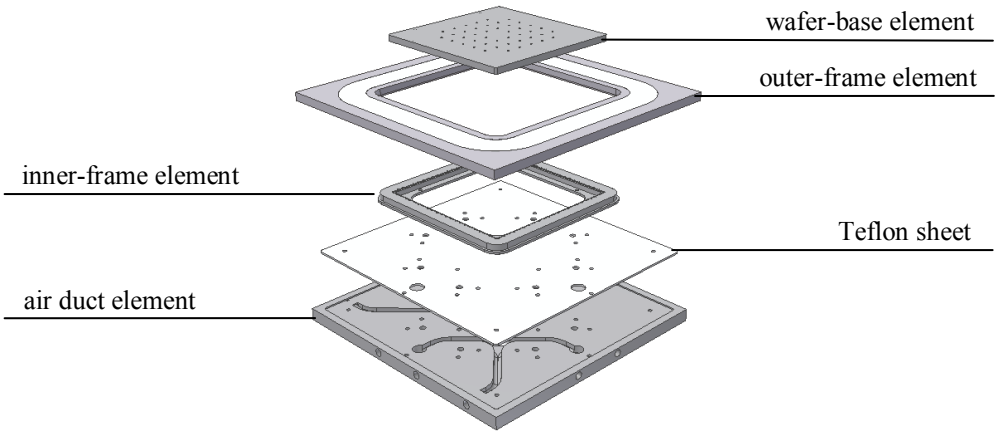

Figure 3-12: Explode view of the assembly device. It is composed by five units: the wafer-base; the outer frame; the inner frame, the Teflon sheet and the air duct element.

3.2.2. Outlet stream improvement

To ensure a homogenous pressure increase in the inner region during the overpressure procedure step, an equal outlet mass flow of the nozzles is required. To assure this, the complete air duct had to be studied. Several air flow simulation with the Ansys CFX computational fluid dynamic software were done and afterwards adjustments on the respective elements.

3.2.2.1. Fundamentals of Fluid Dynamics and CFD

To predict the behave of a fluid flow when submitted to diverse conditions, it is necessary to translate it into an analytical language. The main equations that describe a fluid flow are the Navier-Stokes equation, the continuity equation and the energy conservation equation.

The **Navier-Stokes equation** is the momentum equation for an infinitesimal continuum element dV according to Newton's second law. It is a nonlinear partial differential equation and it accounts for surface forces, viscous forces and body forces. As the forces are balanced for the continuum element dV, they can be considered as an extension of the Euler equation by adding the viscous forces due to internal friction. It is valid for stationary as well as for transient problems. For a Newtonian fluid with constant viscosity η and constant density ρ under isothermal conditions (T=constant) the Navier-Stokes equation can be written in it vector notation:

$$\rho \cdot \left[\frac{\partial \vec{v}}{\partial t} + \left(\vec{v} \cdot \nabla \right) \vec{v} \right] = -\nabla p + \eta \nabla^2 \vec{v} + \rho \vec{f}_{body} \tag{3.2}$$

where the five terms that compose the equation have the following definition:

$\partial \vec{v} / \partial t$ is the transient term.

$\left(\vec{v} \cdot \nabla \right) \vec{v}$ is the convective term.

$\eta \nabla^2 \vec{v}$ is the viscosity term.

$\rho \vec{f}_{body}$ describes the body force term.

∇p is the pressure gradient.

The **continuity equation** describes the fact that the mass change inside a volume element corresponds to the mass flow into or out of the volume element.

$$\frac{\partial \rho}{\partial t} + div\left(\rho \vec{v}\right) = 0 \tag{3.3}$$

For an incompressible fluid the density ρ is constant and the equation becomes:

$$div\,\vec{v} = 0 \tag{3.4}$$

The **energy conservation equation** provides a differential equation for the temperature distribution consisting of a balance of heat and mechanical energy. Hence this equation only is relevant for non-isothermal conditions.

$$\rho \frac{\partial e}{\partial t} + p \cdot \nabla \vec{v} = \nabla\left(k \nabla T\right) + \phi \tag{3.5}$$

where the single expressions consist of the following term:

$\frac{\partial e}{\partial t}$ is the change of the inner energy

$p \cdot \nabla \vec{v}$ is the work due to expansion or compression

$\nabla\left(k \nabla T\right)$ is the heat input due to thermal conductivity

ϕ is the source term

Since the majority problems are too complex to be solved analytically, numerical methods such as Computer Fluid Dynamics (CFD) have been developed. Among others, the objective of CFD is to solve the full three dimensional Navier Stokes equation of a given fluid dynamical problem.

Between the two more common solution methods, Finite Difference Method (FDM) and the Finite Volume Method (FVM), the solution method used at this simulation program, Ansys 13 – CFX, is bases on the second, FVM. This method uses a numerical approximation procedure based on the discretization of the problem by a computational grid. The introduction of its correct attributes (grid size; solution convergence; appropriate mesh; no violation of the conservation equations; and numerical solutions with physical sense) are from essential importance, since they determine the calculation time as the accuracy of the solution.

3.2.2.2. Inner air-flow Simulations

For the simulations in this work merely steady-state solutions were used. Although its solution accuracy can be slightly affected due to ignoring the time variable, they were admitted as sufficient for this study. Besides that, this way of simulation is much faster than transient simulations.

First the boundary conditions for the simulation were defined. Here the inlet air pressure was arbitrary but with consciously chosen to be $p_{in} = 2\,\text{bar}$. The outlet air pressure was at atmospheric pressure, which is equivalent to $p_{out} = 1{,}01325\,\text{bar}$. To notice is that this does not corresponde exacly to reality, since the pressure is going to increase with the time till a certain pressure limit is reached. However this is an acceptable simplification of the problem, because if the air mass is flowing uniformly out of the nozzles at atmospheric pressure, it can be deduced that the air mass flow rate will remain uniform for all nozzles by increasing pressure. To accelerate the convergence time without losing solution accuracy, the discretization of the geometry were adapted to critical zones such as flow deviations, reductions and interesting relevant zones, such as the nozzles. In these specific zones smaller grid cells were used.

A first simulation on the earlier version of the air duct revealed that the direction of the incoming air flow, who leads to the chamber, does not benefit for a homogeneous out flow rate at the nozzles. Here air chamber and air inlet channel were parallel orientated to each other, connected by a small deviation (see Figure 3-13-left). Since the deviation had no significant influence on the flow direction, nozzles at one side showed higher outgoing flow rates than on the other side. In resume, it was noticed that the directions of the air duct had an important effect on the kinetic flow behavior and hence on the distribution to the single nozzles. Therefore, as illustrated in Figure 3-13, a first improvement relied on modifying its incoming air duct into a perpendicular orientation in reference to the chamber.

Figure 3-13:.Illustration of the earlier designed air duct geometry (left) and the further version (right). The reason for the direction modification was to become an equal air distribution at the nozzles.

Another factor that has influenced the outgoing air flow on each nozzle was its aperture. By changing the nozzles diameter and the nozzle quantity, an adequate simulation of the air duct could be accomplished. Figure 3-14, shows a simulation result after taken into account following air duct improvements:

- Modification of the incoming stream direction;
- Reduction of the nozzles outlet cross section area;
- Adjustment of the nozzles quantity.

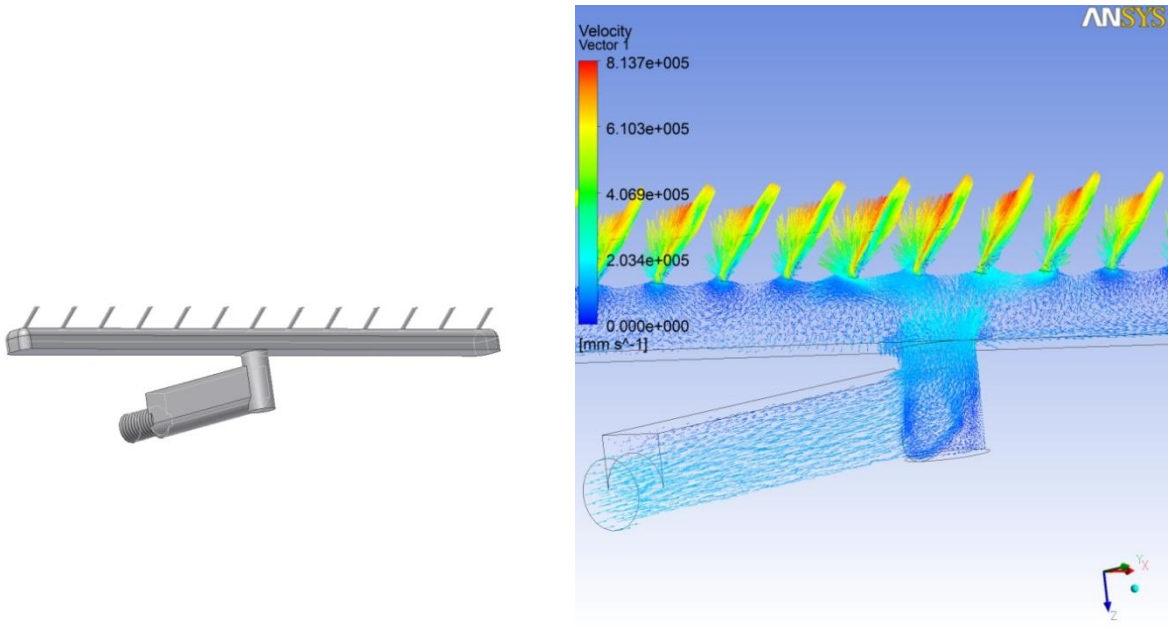

Figure 3-14: CFDillustration of the air duct geometry after its improvement. Negative geometry of the pressurized flow channel with $Ø_{nozzle}$ 1 mm (left). Representation of the vectorial flow velocity of the inner air duct geometry (right).

In Figure 3-14 the equal outgoing air velocity at each one of the nozzles is visible. The arrows show the direction of the air flow and its color the respective velocity at that point (right). From this picture it can be observed that the flow velocity increases to four times inside the nozzles. This is related to the reduction of its cross-section diameter. Moreover it can be observed that the fluid particles, by entering the nozzles, the air stream a turbulent region at the 90° flow shift what deduces to pressure drops in this area. This simulation was made after reducing the nozzle outlet diameter as well as turning perpendicular the incoming air flow direction. Furthermore it is visible that the outlet airflow assume a vertical stream by entering the nozzles, reaching a velocity peak at the of more than $6x10^5$ mm/s. This values are merely simulation values, since it refers to non-compressible air flow. For confirmation, analytically the velocity can be approximately verified due the equation for pressure drop at diffusors, by applying the extended Euler equation:

$$\Delta p = \xi \cdot \frac{\rho}{2} \cdot v^2 \cdot \left[1 - \left(\frac{A_1}{A_2} \right)^2 \right] \tag{3.6}$$

where, Δp is the pressure difference, ρ is the density of the fluid, v is the outflow velocity, whereas A_1 and A_2 represent the outlet and the inlet area, respectively. Moreover ξ is the resistance number in the contraction junction, depending on the shape it varies from $\xi = 0$ for a smoothly rounded junction to $\xi = 0.5$ for an angular junction. More simulation results and respective interpretation, regarding to the flow behavior at the nozzles region, can be reviewed in Attachment A.

Figure 3-15 exposes the four air ducts inside the device after their final improvement. The final version of each air duct was composed by 21 nozzles with a cross section diameter of 1 mm and two inlets. This way it was possible to construct the device more compact without losing accuracy. At the right side of the figure, is illustrated the complete chuck device installed on the mounting plate. To get a more flexible air supply connectivity, it was developed an air distributor, which does the connection of the single suction outlets and the vacuum pump of the workstation.

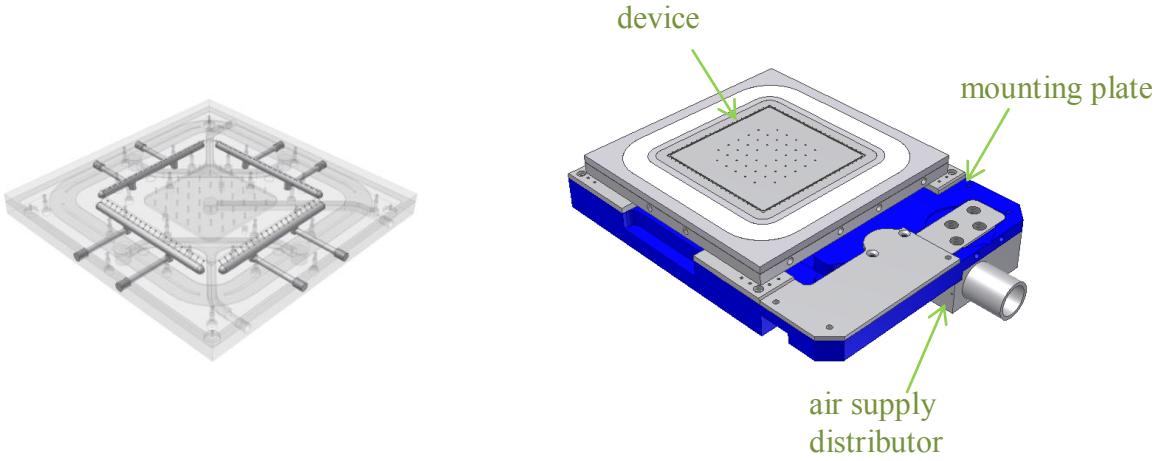

Figure 3-15: Interior render view of the final chuck device after its alterations (left). Perspective render view of the final chuck device placed on the mounting plate (right)

4. EXPERIMENTAL EVALUATION OF THE METALLIZATION CONCEPT

After all components were manufactured the device was tested. In this chapter the experimental buildup of the laser workstation is given, mentioning the principal components and its installation. After contacting the foil onto the wafer, the inner volume was inflated with air. The elevation of the foil in order to the over pressure was measured.

4.1. Experimental montage and controlling

The main part of the experimental procedure was carried out at the laser workstation ILS 500 X from Innolas Systems GmbH. However to accomplish the realization of the experiment, additional components were provided. Apart from the principal components which are needed to execute the process:

- aluminium foil
- silicon substrate wafer
- vacuum pump
- air pressure connection

Two more components came into use,

- pressure regulator
- 4/3-way-air-valve

The first one was necessary to measure and regulate the inflating air pressure. Hence it was possible to achieve relative pressure references. The second was as a complement to switch from suction to overpressure. This way it has allowed to utilize the inner frame also as a suction component, what enhanced the foil adherence during the laser application and enabled a moreover versatile way to explore the vacuum and overpressure functions respectively.

The photograph at Figure 4-1 displays the interior of the laser workstation. Inside constructed chuck device is mounted on the XY motion stage and connected to the air supply.

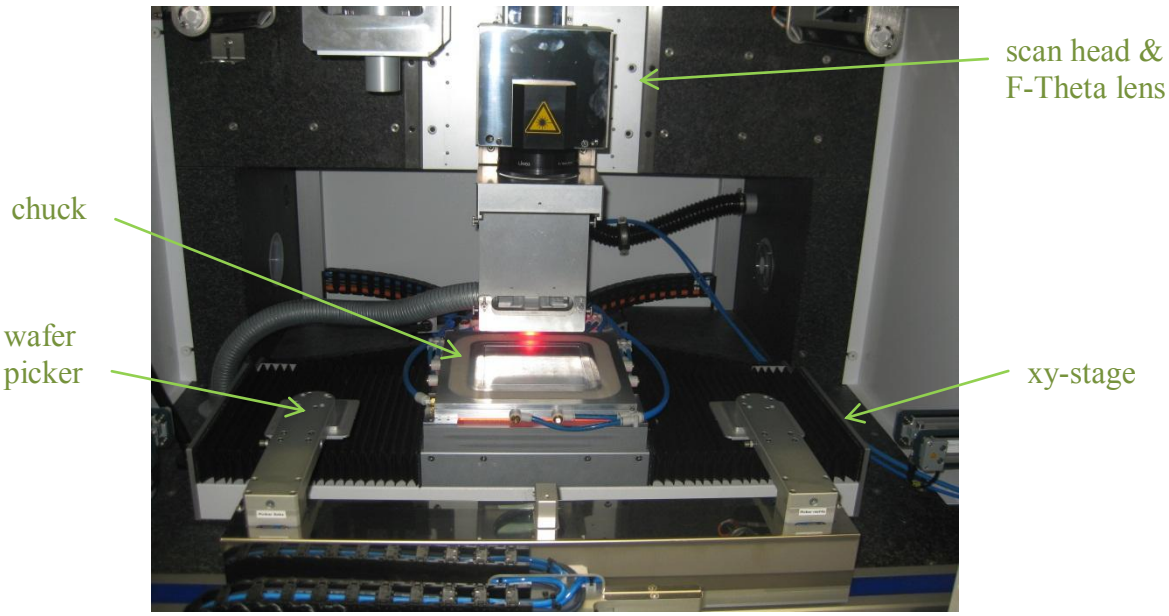

Figure 4-1: Photograph view of the designed chuck, mounted on the laser workstation ILS 500x

The **laser** tool included in the workstation was an infrared spectral range (IR) working disk laser from the Jenoptik Company. This laser has the particular feature to allow for an adjustment of the laser pulse length. This means that the laser pulse length can be adapted to the application, which in this case is to create LFC on aluminum foil. Table 3-1 resumes the laser specifications.

Table 4-1: Laser specifications Jenoptik IR70 [27].

Laser type	Disk IR70
Max. output power	58 W, at 30 kHz
Wavelength	1030 nm
Beam diameter	1,4 mm
Pulse energy	> 6 mJ, at 8 kHz
Pulse repetition rate	8...100 kHz
Pulse length	200...1100 ns

The component that leads the out coming, pulsed, laser beam to the desired position on the substrate is the **scan head.** It is a mechanical component composed by two rotary galvanometer motorized mirrors. Their fast and precise mirror positioning allows the deflection of the laser beam to any specific spot within the working area. This fast scanning component enables to fire 10’000 single contact spots in merely 1 second. In

Table 4-2 are listed some specifications of the used galvanometer scan head from ScanLabs.

Table 4-2: Dynamic specifications of the galvanometer scan head from ScanLab [28].

Type	intelliSCAN 20
Positioning speed	11,0 m/s
Writing speed	340-230 Hz
Tracking error	0,32 ms
Repeatability	< 0,4 µrad
Positioning resolution	0,82 µrad

Another important component on laser processing is the choice of the right incident spot. To collimate the beam into a spot, a **lens** is used and fixed directly to the scan head. For this work it was used a F-Theta lens from Qioptiq. This lens got the particularity that the focus position over the entire scan field is always in the same plane. Table 4-3 notes the most important characteristics.

Table 4-3: Specifications the Qioptiq F-Theta lens [29].

Type	LINOS F-Theta-Ronar
Wavelength	1030-1080 nm
Focal length	254 mm
Working distance	296,2 mm
Maximum scan field	157x157 mm²

For contacting foil per laser small contact spots are preferred, because this offers the possibility to achieve a lower series resistance without lowering the cell voltage. As the lens has a relatively high focal length, to obtain thereupon a small focus spot diameter, a **beam expander** is used additionally. This component has the function to widen up the laser beam diameter before it is collimated by the lens.

At **the workstation** the scan head, combined with the lens, is mounted on a linear ZZ stage. This enables an adequate positioning of its working distance in reference to the wafer substrate. On the other hand the chuck is mounted to a XY axis which allows for moving the substrate in the horizontal plane. Due to high precision requirements, the

whole workstation relies on a solid granite bench, absorbing vibrations and impacts. In Figure 4-2 is simplifying the montage of the laser workstation.

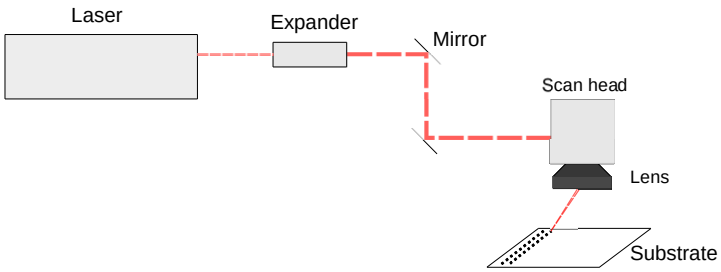

Figure 4-2: Schematic montage of the laser workstation. It is composed by a IR laser source, a beam expander, guiding mirrors, galvanometer scan head including lens and the wafer substrate

The **vacuum pump** used was a side channel blower ESD 220 from Elektror, capable to produce a volumetric flow rate of $\dot{v} = 1{,}5\ \mathrm{m}^3/\mathrm{min}$ at a power of $P = 0{,}75\ \mathrm{kW}$ and a ultimate vacuum of $p = 160\ \mathrm{mbar}$. Previous tests have demonstrated that in this work the optimal pump need to exhibit a high suction volume rate but also a high final vacuum. The first is to compensate for the air leakage between the chuck surface and the foil, which is always present, and the second is to obtain a higher pressure gradient for fixing the foil. The difference between the atmospheric pressure p_{atm} and the final vacuum that is reached between the foil and its surface p_{vac}, represents the vertical pressure force that actually is applied to the foil surface p_{foil} at the same area, which corresponds to the area of the metapor ring A_{ring}.

$$p_{foil} = p_{atm} - p_{vac}$$
$$where\ A_{foil} = A_{atm} = A_{vac} = A_{ring} \tag{4.1}$$

Where A_{atm} is the area of the acting p_{atm}, A_{vac} is the area of the acting p_{vac} and A_{foil} is the area of the acting p_{foil}.

The thickness of the used aluminium foil was 13 µm and had a width of 300 mm. Figure 4-3 shows the process step before firing, when the foil is rolled over the wafer and fixed simultaneously by the suction frame.

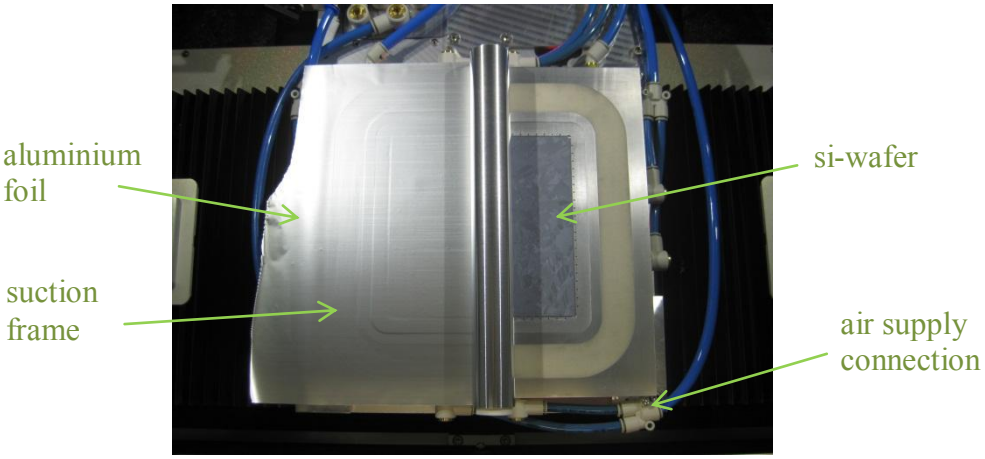

Figure 4-3: Top view during the metal foil lay on step.

The **wafer** used was a full square mc wafer with 200 µm of thickness and the processed lines had a spot pitch of 350 µm.

To obtain a higher evaluation range, it was opted to displace the contact lines at variable distances. Hence the pitch between them was increased continuously by an increment of 100 µm. It started by a line interval of 0,1 mm and ended at an interval of 3 mm. In total there were 29 lines. Pictures of the contact lines such as single spots can be seen in Figure 4-4.

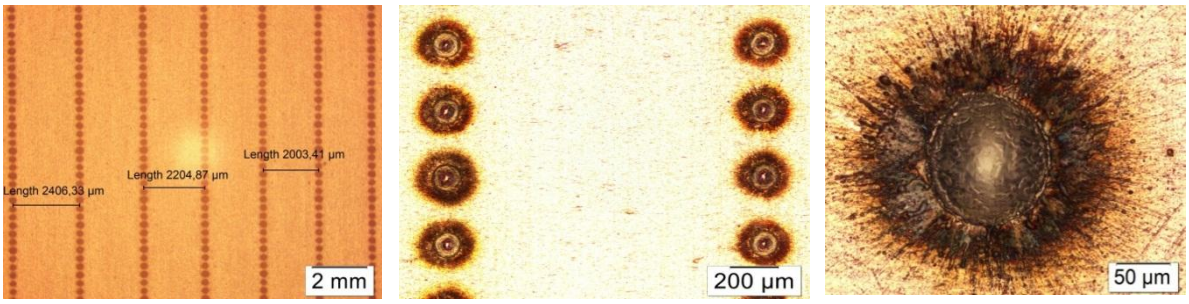

a) b) c)

Figure 4-4: Microscope pictures of the sample at resolutions $\mathbf{1}$, $\mathbf{25}\boldsymbol{x}$, $\mathbf{10}\boldsymbol{x}$ and $\mathbf{50}\boldsymbol{x}$, respectively a) Visualization of the increasing distance between two contact lines $\boldsymbol{L_{line}}$ with incremental of 100 µm to the next; b) Closer view in-between two contact lines; c) Single contact view, ø ca. 110 µm.

After processing the lines, air was blown in between wafer and foil (Figure 4-5). The air pressure inside the volume has been regulated with a pressure regulator. It started at first by low pressure $p_{rel} = 0{,}1$ bar , increasing this until the foil could not hold its isolating properties.

To secure a higher end pressure capacity during this process, it was chosen to use two of four available chambers as reinforcement of the foil suction quality and the ones that are perpendicular to the contact lines for air blowing. This way, the out streaming air from the nozzles was directly guided to the intervals in-between the lines. However, during the foil appliance, the outer frame such as the inner frame, were used for suction. This shifting was managed with the 4/3-way-air-valve.

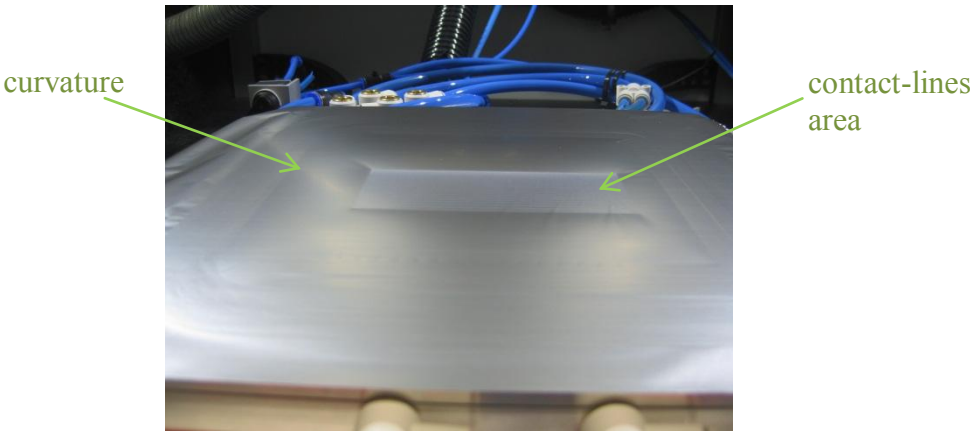

Figure 4-5: Photograph view of step to build up an overpressure.

By this procedure, the maximum achievable pressure was at $p_{rel} = 0{,}2$ bar.

4.1.1. Measurements of the foil elevation

Since the curvature of the foil was, at the interesting zone, not well visible to the bare eye, to evaluate the process and measure the elevation of the foil, measurements with a high dynamic laser sensor were performed. Hence it was used a micrometer precisely distance sensor, type optoNCDT 2300 from the company Micro-Epsilon Messtechnick GmbH. This diode sensor operates based on a laser triangulation principle. Here a visible light spot is projected onto a measuring material surface and its reflected light is imaged onto a position-sensitive element. During the measurement, by changing its spot position, it changes the image on the receiving element and its displacement gets evaluated. Table 4-4 informs about the sensor's specifications.

Table 4-4: Specifications of laser-sensor optoNCDT 2300 [30]

Modell	ILD 2300-20
Measuring Ranges	20 mm
Resolution	0,3 µm, at 20 kHz
linearity	±0,02 % F.S.O.[5]
Measuring rate	1,5 ... 49,02 kHz

The sensor was installed at its focal distance of 50 mm, with reference to the top surface of the metallized sample. The stage drove thereupon orthogonal, and with a velocity defined to be 1 mm/s, to the stripe lines. This way it allowed for a precise measurement of the sensor overrunning, scanning and recording the whole sample, by sending back the respective displacement. As so the sensor frequency rate was defined by $f_{sensor} = 2{,}5$ kHz. This way it did possibly a good measurement resolution.

At the next subchapter the evaluation of the measurement result is made and first conclusions are taken.

4.2. Measurement evaluation and discussion

The resulting experimental measurements are here discussed. The sensor responded with nearly 120'000 points by each measurement. Furthermore, to minimize errors each measurement was repeated two more times, whereof the average was taken.

An effect that was not taken in consideration from the beginning was that while the air pressure was elevated, at some point the contact spots started to breakaway at the edges of the outer contact-lines. This originated the separation of the foil from the wafer. Primarily it started at the corners of the contacted areas, the points are the ones that suffer most load. With an adhesive bounding the maximum reached air pressure was at about 0,3 bar above the atmosphere pressure. At 0,4 bar the foil started with delamination.

Each needle visible in the graph (Figure 4-6) must be seen as an artefact and it represents the contacts, where laser beam passed over, causing at these points measurement disturbance due to rough surfaces what consequently deflected the sensor beam.

[5] F.S.O. – of full scale output

At higher distances the contact artefacts disappear, however by knowing the axis speed of 1 mm/s, it is possible to determine the position of the spots.

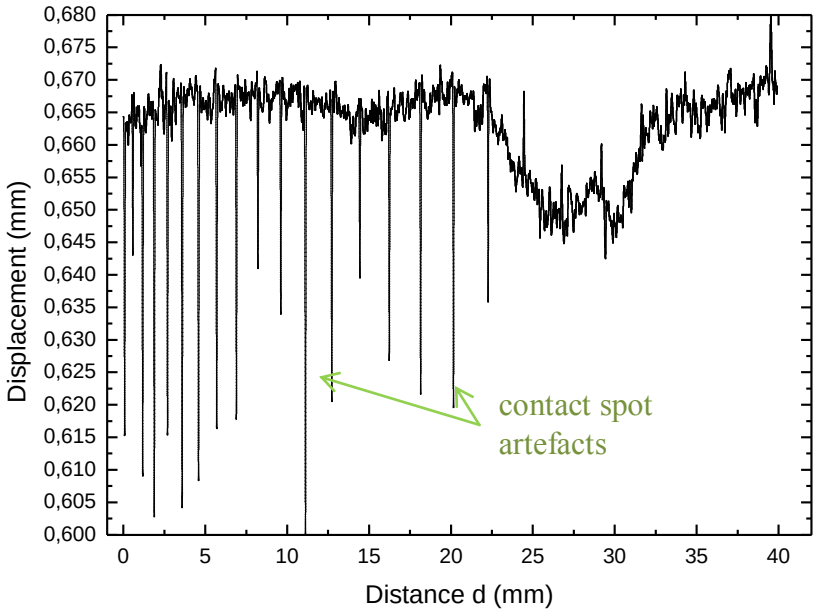

Figure 4-6: Measurement output in case of no air inflation ($\boldsymbol{p_{rel} = 0\ bar}$). This response is used as a reference for the further data.

At Figure 4-6 it is represented the reference measurement by the time that no air pressure was applied. Primarily visible are the artefacts, which allow to determine the location of the contact spots. It is also visible that the gap between the artefact increases, what leaves no doubt that it must be a measurement disturbance while scanning over the single contacts.

The line between the contact artefacts represents the foil surface of the measured region. Due to the measurement accuracy and the small unit of measurement it is difficult to take out clear information. However it is important to mention that the sensor made an absolute mensuration in between 20 mm, what corresponds to the measuring range. Hence it also means the graph is upside down. Having this in mind the artefacts will indicate up, what is more a proof of measuring disturbance at those points. The represented cavity between $d = 23$ mm and $d = 33$ mm, what in fact is something like an elevation (with approx. 20 µm) is in my opinion a defect from the wafer, though it was not visible during the measurements.

The next measurements records were made by initiating to inflate the inner domain. It started with $0{,}1$ bar, followed by $0{,}2-$ and $0{,}3$ bar above atmospheric pressure.

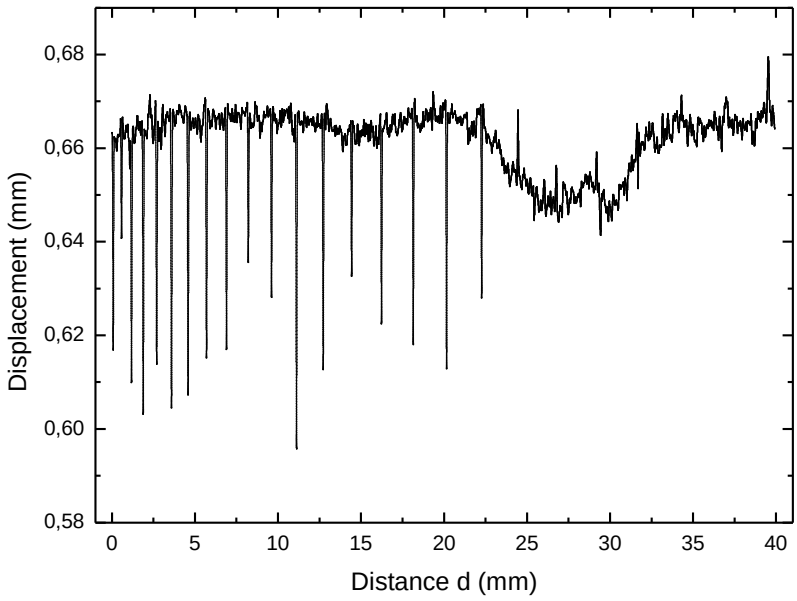

Figure 4-7: Measurement output for the reference when inflated air pressure is $\boldsymbol{p_{rel} = 0{,}3}$ **bar.**

The Figure 4-7 demonstrates the recorded measurement for 0,3 bar relative. At the first view, there seem to be no difference between this one and the measurements without air supply. The artefacts maintain as do so the cavity. A significant foil elevation between the lines is likewise not notable. The best way to find out if the foil has suffered any deformation is to subtract both measurement recordings.

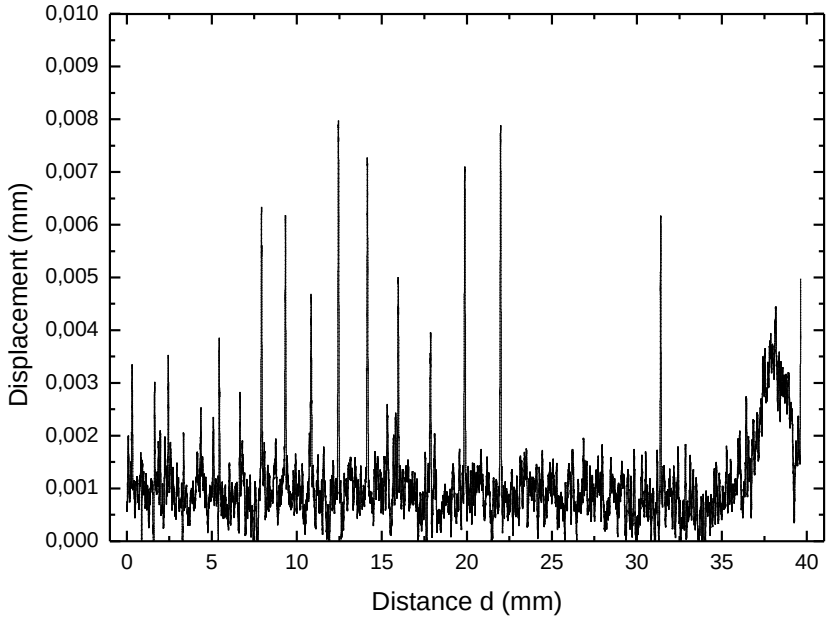

Figure 4-8: Result of the difference between non-air supply and pressure of $\boldsymbol{p_{rel} = 0,3\ \mathbf{bar}}$.

Figure 4-8 represents the difference between the measurement of the highest reached pressure domain and the reference domain, which is without air supply. Even at this graph the artefacts are well visible, which means that their amplitude must have changed measuring at one way and at the other.

Although the small line gaps definitely do not show any curvature by introducing air till 0,3 bar , it is observable that the outcome of the difference calculation not 0 µm is, but yet 1 µm. This can have two reasons. Either the foil has elevated overall 1 µm in reference to sample, or it does represent a measurement offset due to the vibrations caused by the stage motion. Figure 4-9 represents an approach of a small line gap interval, with a contact pitch of $d_{pi} = 0{,}8$ mm. Here it is recognizable that it does not manifest a significant foil elevation during the three pressures phases.

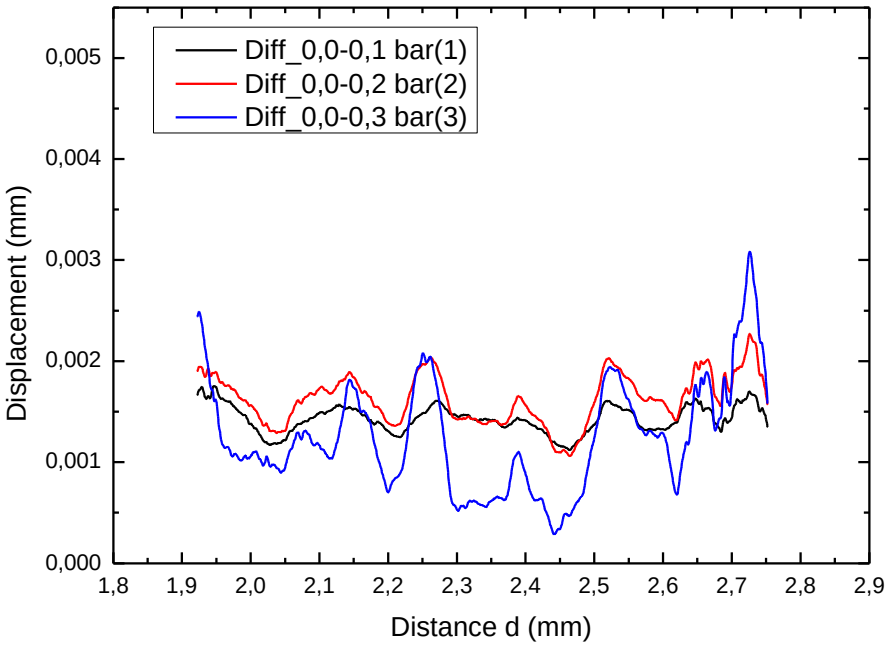

Figure 4-9: Disparities of foil elevation relating to contact pitch of $\boldsymbol{d_{pi} = 0,8\ mm}$.

Even though the measurements of the higher line intervals are less relevant, they still are interesting. It shows graphically an elevation of nearly 5 µm at the right end. By a scanning velocity of $1\ mm/s$ it is possible to determine the contact pitch this elevation is referred to. It belongs to the contact interval of $d_{pi} = 2{,}8\ mm$. Focusing on this last measurement, Figure 4-10 shows an approach to that measured field.

The graph below is an approach of Figure 4-8 between $d = 36\ mm$ and $d = 40\ mm$. It shows the curvatures with changing pressure in order to the reference $p = 0{,}0\ bar$. It is visible that the displacement increases with the pressure domain. More precisely, the black curvature, that represents $0.0\ bar - 0.1\ bar$ reaches a peak displacement of 2 µm, whereas the red curvature reaches the 2,5 µm and the blue curvature, which represents $0{,}0\ bar - 0{,}3\ bar$ reaches even the 4,5 µm of displacement. Though, it is important to mention that this elevation was only once observable in a total of two distinct measurements.

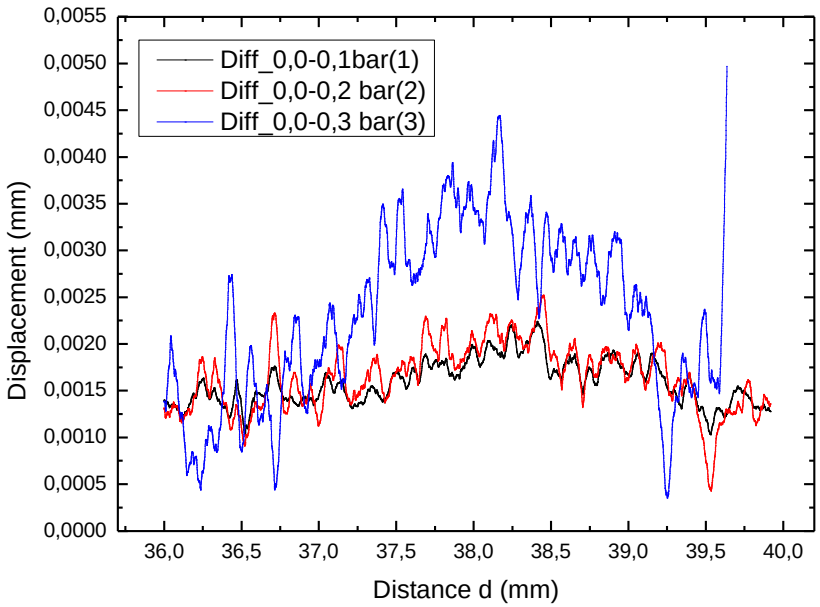

Figure 4-10: Disparities of foil elevation relating to the contact pitch of $\boldsymbol{d_{pi} = 2,8\ mm}$. The foil increases from 2,0 µm up to 4,5 µm.

It also has been tried to heat the foil surface while pressurizing the inner volume, in the hope that the foil would stretch, but the foil delaminated immediately even by a heat addition of $T = 40°C$.

The measurements and its evaluation showed that it was nearly impossible to create a deformation on the foil for small contact-line intervals. At least for this accomplished pressure values. By the largest line gaps it was possible to observe a slight elevation, with a maximal displacement on the middle of the curvature of 4,5 µm though this result should not be considered as reliable. More interval approaches are visible in Attachment B.

5. CONCLUSION AND OUTLOOK

Within the framework of this thesis work, a device has been developed for the implementation of a novel metallization process applicable for the back-contact solar cells. The first experimental tests have demonstrated that there is no significant foil curvature visible between nearby contact lines for inflating relative pressures till 0,3 bar. One reason for this is the maximal inflated pressure that is capable of creating an air gap between foil and the substrate. However, it can still be tested in other experimental conditions and further improvements can be made.

Moreover, at 0,3 bar relative pressure, the pressure limit in this experimental condition was reached and the points of contact between the foil and silicon wafer were peeled off the substrate. Experimental results showed that the adhesion of these contact spots can be improved by the use of a laser tool with shorter pulse length (< 200 ns).

Another major problem is the weak suction created by the outer frame of the chuck. Until $p_{rel} = 0{,}2$ bar, the frame holds the foil stable, while air can be added into the inner volume where the wafer is placed. Above this pressure, the foil starts to lose the adhesion. One possible solution would be to improve the vacuum quality of the chuck, since the metapor material causes a high pressure drop due to its small pores diameter. Another component that could enhance the adherence of the foil would be a pump with a higher final vacuum. With these modifications, it seems to be possible to reach a higher overpressure than 0,2 bar relative.

Furthermore, thinner foils for example, with a thickness of 8 µm or even 6 µm, could be tested. This way, the material can reach its plastic deformation at lower pressure values.

Another idea would be to inflate the foil with warm air, or even to fire the contact holes with higher laser power. The expectations are that, for both alternatives, the foil would expand due to thermal deformation.

In summary, in order to enhance plastic deformation of the foil between the contact lines, higher final pressures need to be reached in the inflating domain. This can be

realized by a stronger foil adhesion, and by the formation of stronger contact between the foil and Silicon.

To finish, this work led to the development and investigation of an alternative metallization technique for c-Si back-contact solar cells by structuring electrodes using metal foils. The designed device has accomplished all its requirements of fixing the foil and creating overpressure domains between the foil and wafer. This allows the elevation of foil areas that are not contacted to the Si wafer after the first laser process. The first experiments showed that the air pressure of 0,2 bar applied for the deformation of the foil was not enough, and applying higher air pressure causes delamination of the contacts. With further experiments focusing mainly on enhancing the foil adhesion and formation of better contacts between the foil and Silicon, the process results are supposed to significantly improve.

REFERENCES

1. Prince, M., *Silicon solar energy converters.* Journal of Applied Physics, 1955. **5**.
2. Christiana Honsberg, S.B. *http://pveducation.org/*. 2013 07.02.2014 - 22:30].
3. Roselund, C. *Interview with Professor Eicke Weber, Intersolar North America's conference committee chair* 2010 03.01.2014 - 10:00]; Available from: http://www.solarserver.com/solar-magazine/solar-interviews/solar-interviews/interview-with-professor-eicke-weber-intersolar-north-americas-conference-committee-chair.html.
4. Bequerel, A.E., *Compt. Rendus de L´Academie des ciences 9* 1839. p. 561.
5. Stuart R. Wenham, M.A.G., Muriel E. Watt, Richard Corkish, *Applied Photovoltaics*. Second Edition ed. 2007: Earthscan.
6. Würfel, P., *Physics of Solar Cells - From Principles to New Concepts*. 2005. 388.
7. Goetzberger, A., J. Knobloch, and B. Voss, *Crystalline silicon solar cells*. 1998, Chichester, UK: John Wiley & Sons Ltd. 254.
8. Blakers, A.W., et al., *22.8% efficient silicon solar cell.* Applied Physics Letters, 1989. **55**(13): p. 1363-5.
9. Nekarda, J., *Laser Fired Contacts LFC*, in *Fakultät für Physik*. 2012, Universität Konstanz: Konstanz.
10. Green, M., *The path to 25% silicon solar cell efficiency: History of silicon cell evolution.* Progress in Photovoltaic: Research and Applications, 2009. **17**: p. 183-189.
11. Nold, S., *Wirtschaftliche Bewertung verschiedener Technologieschritte zur Herstellung hocheffizienter Silicium-Solarzellen*, in *Fakultät für Wirtschaftswissenschaften*. 2009, Universität Karlsruhe: Freiburg im Breisgau. p. 159.
12. Lars Hamann, L.P., Michael Reuter, Jurgen H. Werner, *Colored ribbons achieve +0.3% module efficiency gain*, in *The 22nd International Photovoltaic Science and Engineering Conference*. 2012: Hangzhou, China.
13. Kray, D., *Hocheffiziente Solarzellenstrukturen für kristallines Silicium-Material industrieller Qualität*, in *Fakultät für Physik*. 2004, Universität Konstanz: Konstanz. p. 152.
14. Knauss, H., et al. *Industrially applicable metallisation wrap through solar cell process resulting in efficiencies exceeding 16 %*. in *Proceedings of the 21st European Photovoltaic Solar Energy Conference*. 2006. Dresden, Germany.
15. Schwartz, R.J. and M.D. Lammert. *Silicon solar cells for high concentration applications*. in *Technical Digest of the International Electron Devices Meeting*. 1975. Washington, DC.
16. Smith, D.D., et al. *SunPower's Maxeon Gen III solar cell: high efficiency and energy yield*. in *Proceedings of the 39th IEEE Photovoltaic Specialists Conference*. 2013. Tampa, Florida, USA.
17. Saueressig, M., *Herstellung und Charakterisierung von Siebdruckformen für die Metallisierung kristalliner Silizium-Solarzellen*, in *Druck - und Medientechnologie*. 2009, Hochschule der Medien, Stuttgart: Freiburg im

Breisgau. p. 65.
18. Neu, W., et al., *Low-cost multicrystalline back-contact silicon solar cells with screen printed metallization.* Solar Energy Materials and Solar Cells, 2002. **74**(1-4): p. 139-46.
19. Menz W., J.M., *Mikrosystemtechnik für Ingenieure*. 2 ed. 1997: VCH Verlagsgesellschaft mbH.
20. Granek, F., *High-Efficiency Back-Contact Back-Junction Silicon Solar Cells*. 2010: Freiburg i. Br.
21. W.P. Mulligan, M.J.C., T. Pass, D. Smith, N. Kaminar, K. McIntosh, and R. M. Swanson, *Solar cell and method of manufacture*, in *US Patent*. 2008: US.
22. Nekarda, J.-F., et al. *Aluminum foil as back side metallization for LFC cells*. in *Proceedings of the 22nd European Photovoltaic Solar Energy Conference*. 2007. Milan, Italy.
23. Schneiderlöchner, E., et al., *Laser-fired rear contacts for crystalline silicon solar cells.* Progress in Photovoltaics: Research and Applications, 2002. **10**: p. 29-34.
24. R. Preu, e.a., *Verfahren zur Herstellung eines Halbleiter-Metallkontakts durch eine dielectrische Sicht*. 2000.
25. Klausmann, S., *Entwicklung und Aufbau einer Pilotenanlage im Labormaßstab zum Anlegen von Metallfolie an Siliziumwafer*. 2010, Karlsruher Institut für Technologie.
26. Horst-Witte, *Vacuum Clamping Technology*. Catalogue 2013.
27. Jenoptik Laser GmbH, *JenLas disk IR50/IR70 l JenLas disk IR70E, IR-Disk Laser, Tunable Pule Length*. 2012.
28. ScanLab, *intelliSCANde, intelliSCAN*: Puchheim.
29. Qioptiq. *F-Theta-Ronar 1030-1080 nm - Fused silica*. 2013 08.02.2014 -23:00]; Available from: http://www.qioptiq-shop.com/en/Precision-Optics/LINOS-Laseroptics-Lenses/LINOS-F-Theta-Ronar-Lenses/F-Theta-Ronar-Lenses-1064-1030-1080-1550-nm.html#popup_4401-288-000-20.
30. Micro-Epsilon, *Data sheet - Laser Triangulation Diplacement Sensors, optonNCDT-2300*.

ATTACHMENT A

Interpretation of the remaining simulation results for the inner air duct improvement. The improvement was necessary to secure a homogeneous stream outlet by the nozzles. After reducing the nozzle diameter and the incoming flow direction, a good approximation to the pretended result was obtained.

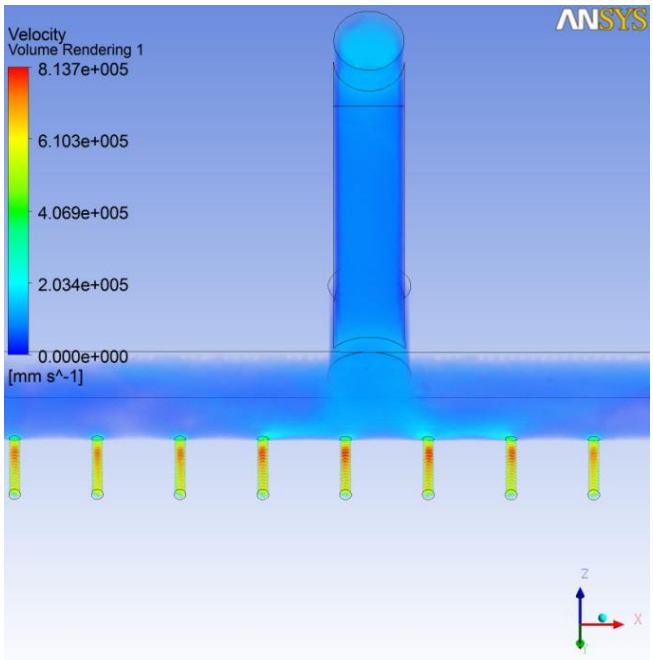

Figure A-1: This figure represents the velocity variation inside the air-duct. The first observation is that the kinetic energy of the fluid increases significantly by the nozzles entrance, when compared with the major geometry. There are two reasons for this: the accentuate reduction of the nozzles cross-section area and the conservation of the mass.

Moreover it can be seen a lowering of the velocity by increasing distance to the inlet channel.

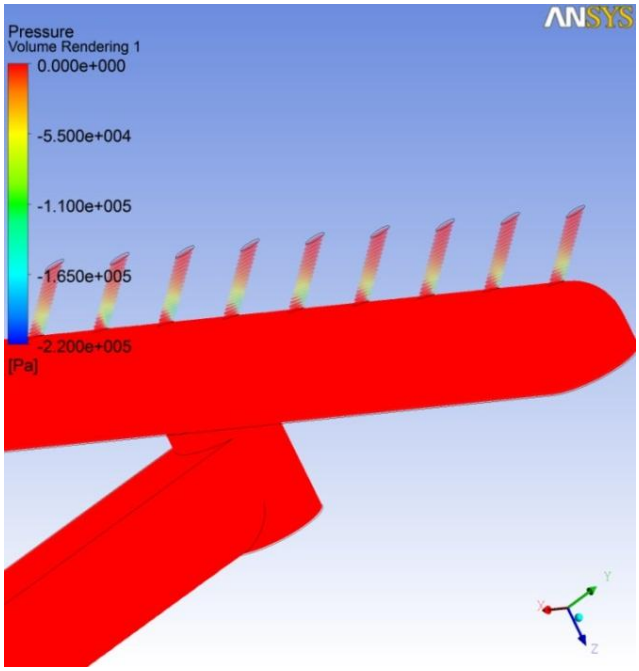

Figure A-2: This graph illustrates the pressure drop at the inner geometry. It shows a negative pressure in the nozzles entrance ($\boldsymbol{p \approx 1,1x10^5\ Pa}$). According to Figure 3-14 this is explained because of the vertical fluid flow direction by entering in the nozzle. A high velocity (Figure A-1) and turbulent region is there to expect. This explains the locally negative pressure.

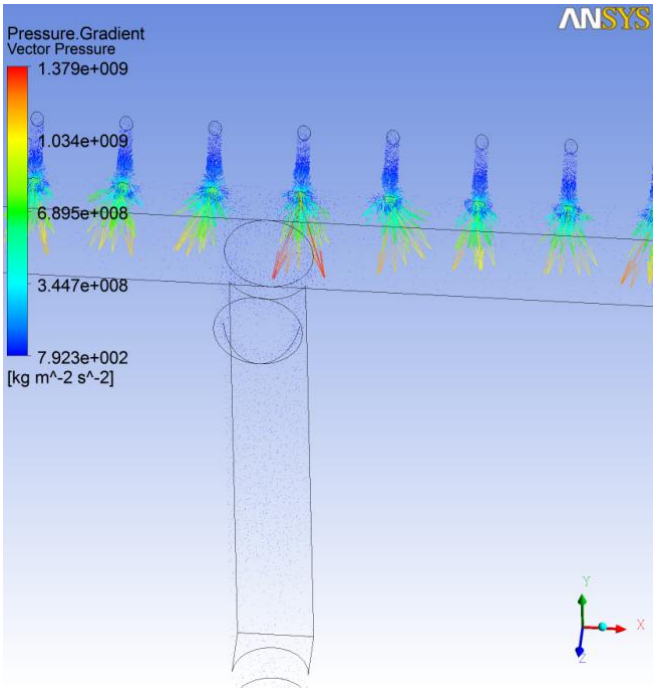

Figure A-3: The figure shows the vectorial pressure gradient in the nozzles area. According to Figure 3-14, it can be interpretated as: in the nozzles, the incoming particles follow a vertical flow and bounce on the upper nozzle wall. Due to the collision with the wall, an immense pressure drop happens in this zone. The vector direction is perpendicular to the nozzle wall. The highest pressure drop occurs at the outlet channel. Here the velocity is maximum and therefore the pressure gradient.

After these simulations, the only modification that has been made in the air duct geometry was to use two inlet channels instead of one (Figure 3-15).

ATTACHMENT B

In this attachment more results regarding to the surface measurement of the aluminium foil, during the inflating procedure are shown. The first a second picture represents the pressure differences of 0,1 bar, 0.2 bar and 0,3 bar by the line gap of 2,1 mm and 1,4 mm, respectively.

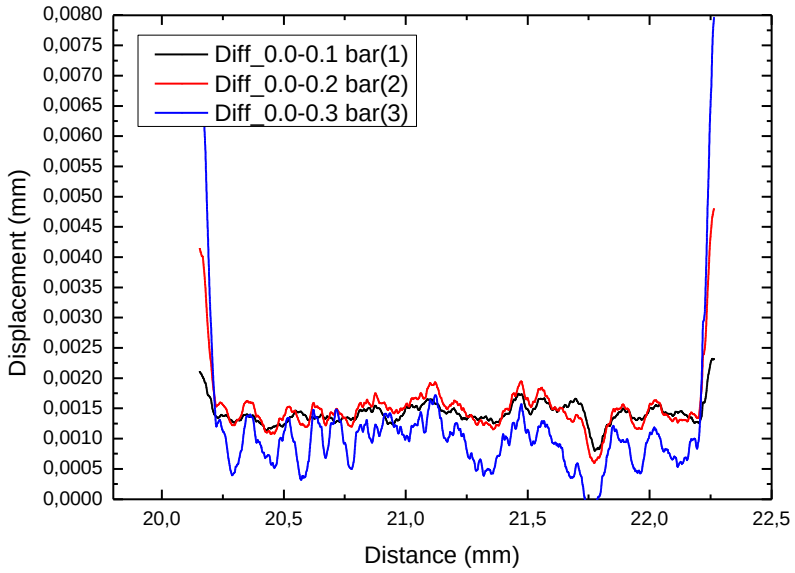

Figure B-1: Disparities of foil elevation relating to the contact pitch of $\boldsymbol{d_{pi} = 2,1\ \mathbf{mm}}$.

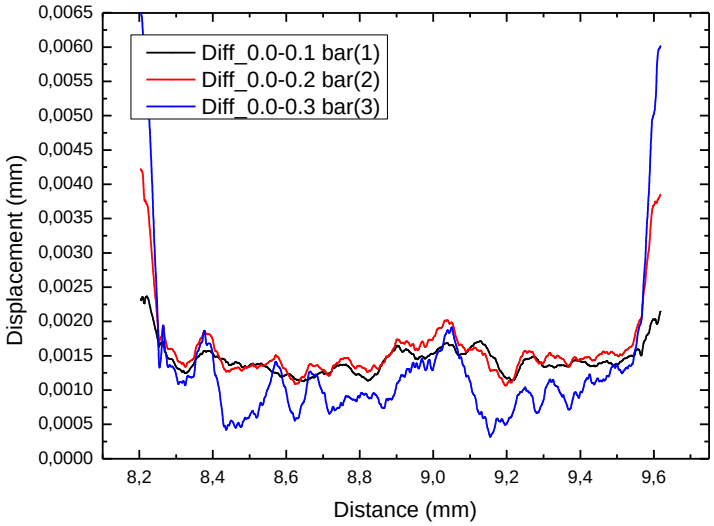

Figure B-2: Disparities of foil elevation relating to the contact pitch of $\boldsymbol{d_{pi} = 1,4\ \mathbf{mm}}$.